Theoretic Investigation on Plasmonics of Noble Metallic Nanoparticles

A THESIS
SUBMITTED TO THE FACULTY OF THE GRADUATE SCHOOL
OF THE UNIVERSITY OF MINNESOTA
BY

Xiaohu Qian

IN PARTIAL FULFILLMENT OF THE REQUIREMENTS
FOR THE DEGREE OF
Master of Science

Advisor: Dr. Jing Bai

August, 2013

© Xiaohu Qian 2013
ALL RIGHTS RESERVED

Acknowledgements

To those who help me up over the years in the department of electrical engineering at University of Minnesota, Duluth, I highly appreciate them and keep their kindness in my memory as long as possible.

First and foremost, I would like to give my deepest gratitude to Dr. Jing Bai, an extremely responsible supervisor with incredible insight in nanooptics related field. Without her support and guide, it is impossible to complete my thesis intime. Her help is not only limited within the academic activity, but extend to my daily life and even my career choice. It was very lucky to have you as my thesis advisor. I also appreciate the research assistantship support from the Grant-in-Aid fund by the Graduate School of the University of Minnesota, and the teaching assistanship support from the EE department at UMD. Tons of thanks goes to Dr. John Hiller and Dr. Mohammad Hasan. It is their penetrating and constructive comments on this thesis that guarantee the quality of it. As a student without any strict training in physics, I have learned how to think a phenomenon in the way of physics from Dr. Hiller's course of quantum mechanics. Dr. Hasan offered me heaps of training in machine learning and pattern recognition, which is very elegant and beneficial to broaden my academic vision. Special thanks has to be ascribed to two of you for joining in the my committee of defense. It is your strict requirements that greatly improve the quality of this thesis. I am also grateful to Dr. Jiann-Shiou Yang, who consistently provides heaps of help to me during my stay at EE; and to Dr. Hua Tang, the discussion with you about my research in biomedical application is very interesting and particularly inspiring to me. It is hard to forget the grace of Ms. Shey Peterson and Ms. Sarah Wilfahrt, both of whom keep on excellent performance in serving hundreds of students, stuff and faculty at EE while never refused to help me out of each problem I encountered.

At last but not least, it is impossible to express my gratitude to my family members, i.e., my wife, parents and grandparents. Your consistent love and unparallel sacrifice to me is priceless and most cherishable. My utmost gratitude goes to my wife-Xiaochen. Without you, my life and this thesis would fail to make any sense. Thank you for your companion, and huge sacrifice for me during these years. Most of all, it is your love, support and encouragement that is incredible and which I am most thankful for.

The list to acknowledge is almost endless, but I have to stop here. Without each piece of your help, there will be one more block on my road to complete this degree thesis.

Memory may fade away, but the fragrance of grace will always stand in my heart.

人法地，地法天，天法道，道法自然。

"The Ways of Human beings are ruled by those of Earth.
The Ways of Earth by those of Heaven.
The Ways of Heaven by those of Tao.
And those of Tao by the Self-so."

— `Laozi`, *Tao Te Ching*

Dedication

To my grandparents, Jun-Ming and Hong-Lian.

Abstract

In this thesis, we report our theoretic investigation on the surface plasmon polaritons of noble metallic nanoparticles and its applications. By means of numerical experiments, we studied the general far-field and near-field optical properties of the promising hollow metallic nanoparticles, the pattern of far-field extinction efficiency and the near-field surface-enhanced Raman scattering. We demonstrated the distribution of plasmon resonance wavelength as functions of the geometrical factor of hollow spherical gold and silver nanostructures. In addition, we utilized a novel mechanism of harnessing the mechanical strain to controllably tailor the plasmon-based optical spectra of single metallic nanospheres and the array of metallic nanoparticle of spheres and circular discs. The second goal of this thesis is to utilize a novel mechanical-strain-induced effect to enhance the light-trapping performance of plasmonic solar cells. This multi-physical scheme has the potential of considerably reducing the thickness of semiconductor layer and hence save the cost of production of the solar cells. Corresponding simulation results demonstrated this strategy is promising to decrease the fabrication budget of solar industry.

Contents

List of Tables

List of Figures

Chapter 1

Introduction

This chapter is dedicated to the introduction of main goals of current thesis, the surface plasmon resonance(SPR) of metallic nanoparticles(NPs). We firstly introduce the general plasmon resonance and its applications. Then we address the hollow metallic nanostructures and their applications. Thirdly, the plasmonic solar cell will be introduced. Finally we will mention the mechanical strain effect on dielectric functions of metallic nanostructures.

1.1 Introduction to Plasmon Resonance

1.1.1 Physical Pattern of Plasmon Resonance

Plasmon is the quantum of a plasma oscillation, to be specific, the eigenmodes of collective oscillations of the quasi-free electrons in metals. Due to the movement of these charged electrons, a character of these oscillations is they are inherently associated with electromagnetic field. Since the different types of boundary conditions determine the modes of plasmons, i.e., bulk, surface or particle plasmons.

This thesis is centered on surface plasmons and particle plasmons of metallic nanoparticles. Surface plasmons are the electromagnetic eigenmodes occurring at the metal-dielectric interfaces, involving charges distribution along the interface and electromagnetic eld in both media. The associated electromagnetic field propagate exponentially in the direction perpendicular to the interface. Fig.(1.1) exemplifies a typical plasmon

standing on the interface of metal-interface. In order to delineate the plasmon resonance and its associated optical properties of metallic nanostructures, we have to proceed into the solid state theory for dielectric functions of metal and electrodynamic model of plasmon resonance, which is the focus of next chapter.

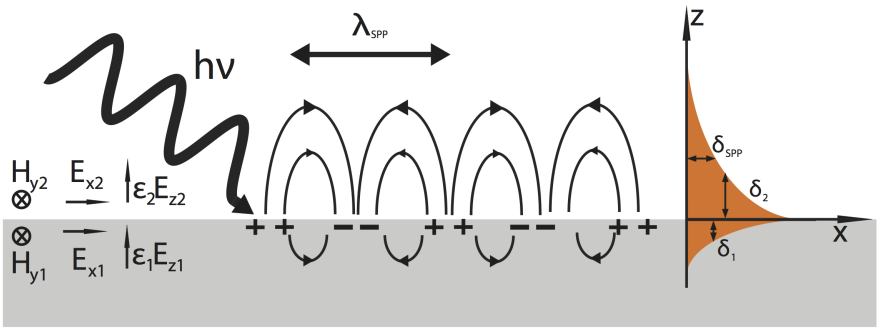

Figure 1.1: Field distribution of surface plasmon resonance from Wikipedia.org [1]

1.1.2 Applications of Surface Plasmon Resonance

It is the existence of a tremendous plethora of application of SPR that triggers us to conduct the research in this thesis. In this section, we will give a short tour in the world of exciting physical and chemical properties and amazing applications of SPR.

The phenomena that metallic nanoparticles exhibit plasmon resonance have given rise to a plethora of mature and potential applications in each field related to nanoscale science and technology [2, 3]. And the progress in synthesis and structural characterization techniques of metallic nanostructures provide the platform to realize all these applications [4]. First of all, a very popular while commonly neglected phenomenon is that SPR is the origin of the colors of metal nanoparticles. In Fig.(1.2), we can observe vastly distinct colors stemming from different hollow gold nanospheres(HGNs).

The most prevalent application for metallic nanostructures plasmon resonance is the surface-enhanced Raman scattering (SERS), which employs the evanescent field at the surface of nanoparticle to dramatically magnify the originally weak but molecule specific Raman signal [5, 6]. Among those applications based on SERS, typical candidates include single molecule sensing and detection [7, 8, 9, 10]. In addition, the absorption and scattering of metallic nanostructures plasmon resonance lead to heaps of biomedical

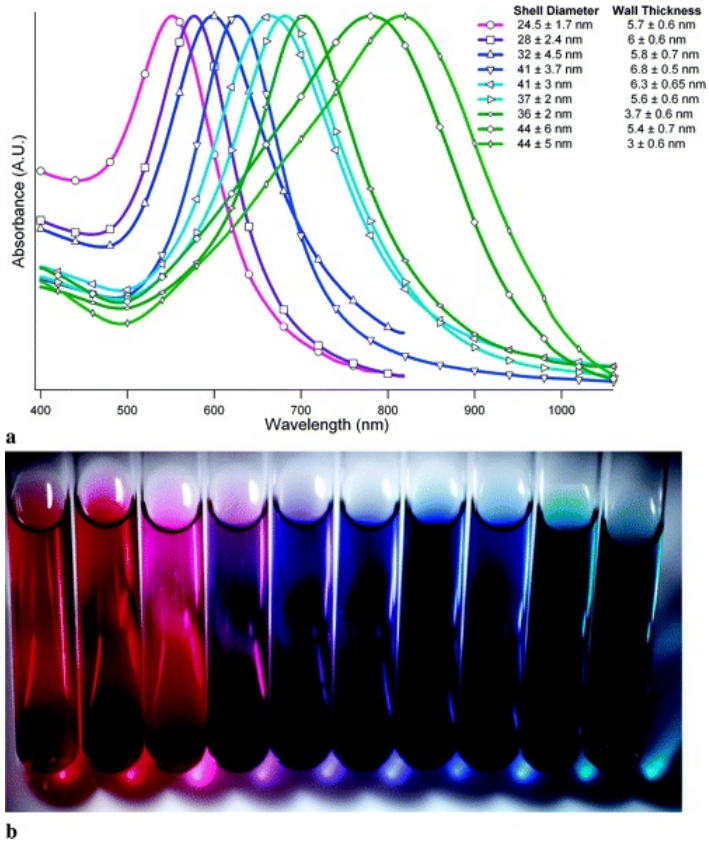

Figure 1.2: (a) UV-visible absorption spectra of nine HGNs samples with varying diameters and shell thicknesses. (b) the color range of HGN solutions, except the left one contains solid gold nanoparticles. Reprinted with permission from A. M. Schwartzberg, T. Y. Olson, C. E. Talley and J. Z. Zhang, *J. Phys. Chem. B* **2006**, *110*, 19935-19944. Copyright 2006 American Chemical Society.

applications such as photothermal treatment for cancer [11, 8, 12], optical sensing and labeling [13], cell-uptake and drug delivery [14], and biomedical imaging [15, 16]. The characteristic localization of SPR also triggers the generation of miniaturized photonic devices [17, 18]. Another application of significant interest appear in the field electron dynamics of nanoparticles, which utilize the fact that electronic properties of a cluster of nanoparticles are much more sensitive to surface changes in conjunction with strong optical absorption [19, 20, 21].

1.2 Introduction to Hollow Metal Nanoparticles

One of the topics we will explore in current research is the optical properties on the basis of the SPR of hollow metallic nanoparticles, thus we now present the introduction to this type of particular NPs.

Hollow metallic NPs are very promising due to the high tunability of their SPR based optical properties [22, 23, 24, 25, 26]. In particular, two types of hollow metallic nanostructures are hollow gold nanospheres(HGNs) and hollow silver nanospheres(HSNs), both of which are composed of spherical shell coated on embedding medium, are getting increasing popularity due to the high degree of homogeneity and, more importantly, superior tunability of their SPR [23, 24, 27, 25]. Correspondingly, we will study the optical properties of the two kinds of NPs in future chapter. The typical structure of a hollow metallic nanosphere is plotted as a schematic image cross section in Fig.(1.3) We note that the surrounding medium is set as water in our research, but in general, it could be reasonably chosen as each suitable material [27].

1.2.1 Applications of Hollow Metal Nanoparticles

Heaps of applications based on the SPR of hollow metallic nanospheres have been demonstrated and are receiving more explorations from every community related to nanotechnology. To this end, people have substantiated the versatile applications of HGNs and HSNs in SERS for molecules adsorbed to both external surface of nanospheres and their interior cavity covered by shell [28, 29], infrared absorption [30], fluorescence [31]. In addition, there are chemical and biomedical applications of hollow metallic nanospheres in catalysis [32], tumor therapy [11], drug delivery [33].

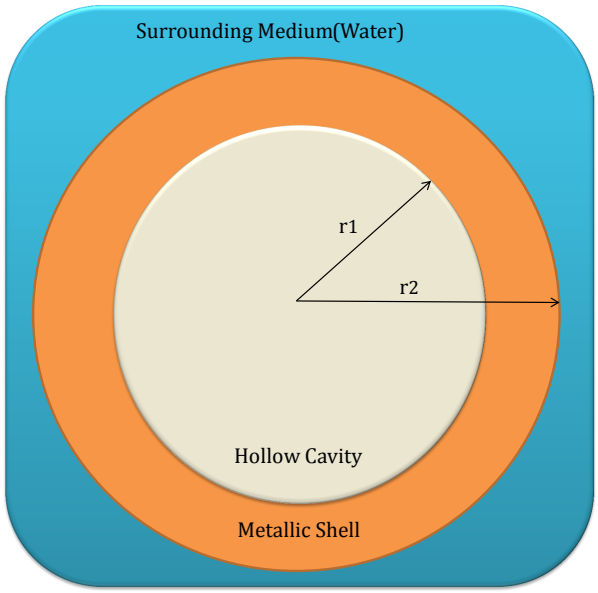

Figure 1.3: The typical geometry of spherical nanoshells.

It is worth to point out that, due to their tiny size and spherical shape, in combination with the intense while controllably tunable plasmonic spectra, HGNs and HSNs are ideally suitable to biological applications which are very selective to the resonance wavelength and geometry of nanoparticle candidates [27, 29]. In order to guarantee the light penetrate the biological tissues without being absorbed by other chromospheres, the plasmon resonance wavelengths (PRWs) of metallic nanoparticles have to fall in the near-infrared region(NIR) [34]. Recently, a series of work by Zhang lab have confirmed that PRWs of well-engineered HGNs can be tuned to cover the NIR [23, 29]. As for the geometry, we note that HGNs and HSNs can be synthesized with sufficiently small size, such as 25 nm diameter [23, 35]; in contrast, it would be difficult for large metallic nanostructures such as gold/silica nanoshells with diameters typically around 100 nm to penetrate the thin cell membrane of biological tissues [29].

An important progress which greatly prompt the understanding of optical properties of hollow metallic nanospheres is the improvement in the synthesis of hollow metallic nanostructures [36, 23, 35, 29]. Both Liang *et al.* [36] and Schwartzberg *et al.* [23] produced HGNs by utilizing Cobalt nanoparticles as sacrificial templates which are

prepared via the method proposed by Kobayashi *et al.* The important contribution of Preciado-Flores *et al.* lies in that they reported a highly reproducible synthesis procedure of HGNs by utilizing polyvinylpyrrolidone(PVP) as a stabilizing agent [29]. Recently, based on nanoscale Kirkendall effect, Moshe *et al.* present a reaction-diffusion process which is capable of shaping the morphology-preserving and single-crystalline HSNs [35].

1.2.2 Motivation of Study on Hollow Metallic Nanoparticles

Though these substantial progresses on the synthesis of hollow metallic nanospheres have been reported, there is still lack of sufficient guide from theoretic study on how the optical properties of hollow metallic single-shell nanospheres vary with their geometrical parameters change. The hybridization theory serves as an effective tool of analyzing the plasmon resonance of nanostructures but it is only valid within quasistatic limit, which means that it can not predict any size-related effects [37, 3]. In addition, we note that Tam*et al.* [38] conducted the study on the plasmon resonance of extremely large gold/silica nanoshells with focus on dipole plasmon wavelengths. A recently reported work we note is the theoretic analysis of SPR in hollow bi-metallic double-shell nanospheres [27], where the authors utilized the extended Mie theory to determine the SPR-based optical properties of bi-metallic double nanoshell.

The crucial point of current investigation lies in that because the SPR-based optical properties of hollow metallic single-shell nanospheres, such as absorption and scattering, are essentially governed by their geometrical factors and thus dominate the applications of this type of unique nanostructure, it is of considerable interest to investigate the underlying principles of how their optical properties respond to the variation of geometrical factors. In doing so, we aim to provide a delicate insight and effective guidance for the parallel experimental and industry efforts and hopefully trigger more possibilities of tailoring the optical properties of hollow metallic nanospheres.

1.3 Introduction to Plasmonic Solar Cell and Strain Effect

1.3.1 Introduction to Plasmonic Solar Cell

A solar cell is a promising device that converts the energy of light into electricity by photovaltaic effect, and hence it has the potential of solving the problem of climate change and energy conversion. Currently, solar cell industry is dominated by crystalline silicon substrate with thickness 200-300μm. As a result, the cost of solar cell primarily depends how much silicon materials is used in solar cell production. In order to reduce the cost, a simple and direct approach is to use thinner semiconductor layers on condition that the associated loss of performance is desired. Actually it is the demand of lower material consumption that lead to the birth of thin-film solar cells, or second generation solar cells [39]. In addition, for bulk recombination-dominated semiconductors, thin-film solar cell are found to have better carrier collection and reduced bulk recombination, both of which enhance the solar cell efficiency [40]. However, the absorption efficiency of thin-film solar cell are also reduced when the frequency of light is approaching the electronic bandgap of silicon, or other substrate semiconductor. Similarly, this bottleneck naturally demands a effective scheme offering high-efficiency light-trapping performance without thick semiconductor absorption layer. Thanks to the existence of SPR, which can localize, or in other words, trap the light within a thin layer close to the interface between metallic particles and semiconductor substrate, people originate the combination of the well-engineered metallic nanoparticles or nanoparticle array and traditional thin-film solar cell form a novel generation solar cell, i.e., plasmonic solar cell [41, 42, 43]. In Fig.(1.4), we demonstrate the typical configuration of a PSC.

There are three SPR-based light trapping techniques available for minimizing the thickness of semiconductor layers in thin-film solar cell, which can still maintain the sufficiently high optical absorption and hereby the efficiency of conventional thin-film solar cell [41]. The first one is to harness the intense scattering from metallic naoparticles at the surface of thin-film solar cells, which is simple in terms of fabrication and adopted in my thesis for study. Secondly, the light trapping is realized by means of the excitation of localized surface plasmons in metal nanoparticles embedded in the semiconductor layers. The final scheme is similar to the second while it differs in that the excitation of SPR occurs at the metal-semiconductor interface. The detailed mechanism

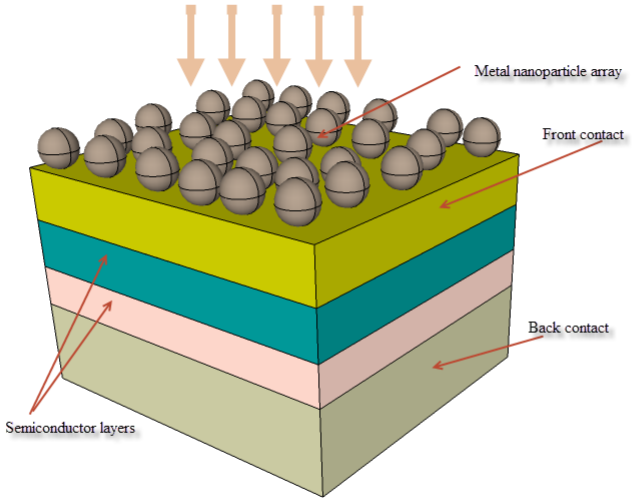

Figure 1.4: Sketch of a typical PSC.

and demonstration of the three techniques can be tracked in [41].

1.3.2 Motivation of Study on Strain Effect of Plasmonic Solar Cells

As we have just discussed, PSCs host huge potential of reducing the cost of fabrication of solar cells. Thus we are just wondering is there additional method of further reducing the cost of PSCs. Since the key issue of PSC lies in their light-trapping capacity, if there is an approach permits us achieve higher light-trapping index with same semiconductor layers, it means we can use thinner semiconductor layers in PSCs to obtain the original light-trapping index. In other words, we are able to further reduce the cost of solar cells.

Fortunately, in 2009 Qian and Park proposed a novel mechanical-strain-induced methodology of controllably tailoring and, more important, enhancing the SPR spectra of gold nanosphere [44]. This methodology is then extended to face-centered cubic(FCC) metall nanoparticles with typical regular geometry such as sphere and cuboid [45, 46]. To put it simply, people have confirmed that dielectric functions of nanoscale metal is subject to surface-damping effect [47, 48] and lattice-deformation effect [49, 50]. The strain effect is a combination of the two effects. In Chapter 2, we will make a detailed

presentation of this methodology.

1.4 Structures of Thesis

The specific goals of each chapter of this thesis are given as following:

Chapter 1 focuses on the introduction of applications and motivations of surface plasmon resonance of metallic nanoparticles, hollow metallic nanoparticles and plasmonic solar cells. Finally we list the main goals pursued in each chapter of this thesis.

Chapter 2 begins with addressing the theory of surface plasmon resonance of nanoparticles. Then detailed formulation of Mie theory are presented with two case. Finally we introduce the novel methodology of applying the mechanical strain into dielectric functions of metal nanoparticles.

Chapter 3 reports our analysis of the far-field and near-field optical properties of hollow noble metallic nanoparticles.

Chapter 4 presents the novel methodology of utilizing mechanical strain to tune the optical properties of nanoparticles and enhance the light trapping performance of plasmonic solar cell.

Chapter 5 summarizes the topics under study in this thesis.

Appendix A lists the glossary and acronyms used in this thesis.

Appendix B introduces the numerical methods employed to calculate the results analyzed in this thesis.

Appendix C gives dielectric constants of gold and silver which are crucial to our research.

Appendix D includes a sample Matlab code to exemplify our calculations of optical properties of metal nanoparticles.

Chapter 2

Theoretical Background

In this chapter, we will present several analytical theories of SPR and strain effect on SPR of noble metal NPs.

2.1 Basic Theories of Plasmon Resonance

We firstly will introduce the Drude-Sommerfeld model of metal, which is important to understand many properties, particularly the optical properties of metal. Then we present the core electrodynamic relationship of surface plasmon resonance, which is essential to define this particular phenomenon. Finally we introduce some widely used terms in optics which will be used in this study to describe the SPR-related optical properties of metallic nanoparticles.

2.1.1 Drude-Sommerfeld Model of Metal

In this theory, the metal is treated as a gas of independent and volumeless electrons, which freely move with collisions occurring at the period of electron relaxation time. Many physical properties of metals, including optical properties, can be well described by this frequency-dependent dielectric function, which is commonly expressed as a sum of two terms [51], one for the free or conduction electrons, and the other term representing the core or bound electrons [52, 44]

$$\varepsilon_{bulk}(\omega) = \varepsilon_{core}(\omega) + \varepsilon_{free}(\omega) - 1, \tag{2.1}$$

where the free electron term $\varepsilon_{free}(\omega)$ is written as

$$\varepsilon_{free}(\omega) = 1 - \frac{\omega_p^2}{\omega^2 + j\gamma\omega}, \tag{2.2}$$

where j represents the square root of -1 throughout this thesis until otherwise stated, ω is the angular frequecy of incident light, plasma frequency $\omega_p = (Ne^2/\varepsilon_0 m_{eff})^{1/2}$ relies on the electron density N and effective mass m_{eff}, and γ is the bulk damping constant, which is pertinent to electron scattering processes. Please note that ε_{core} and ε_{free} originate from interband and intraband transitions, respectively [52]. We now list all the necessary parameters for determine the Drude-Sommerfeld model of the dielectric functions of gold and silver nanoparticles in Table(2.1), which will be defined later in Section(2.3) where we address the mechanical strain effect on dielectric functions of metallic nanoparticles.

Table 2.1: Parameters of dielectric functions

Material	A	v_F	$1/\gamma_0$	m_{eff}
Au	0.13 [53]	1.41×10^6 m/s [54]	9.3×10^{-15} s [55]	$0.99 m_{electron}$ [55]
Ag	0.25 [56]	1.39×10^6 m/s [54]	31×10^{-15} s [55]	$0.96 m_{electron}$ [55]

2.1.2 Electrodynamic Theory of Surface Plasmon on Planar Interface

In terms of electrodynamics, simply speaking, the core issue of understanding surface plasmon along metal-dielectric interface lies in the dispersion relation equation involving the lateral momentum $k_{||}^2$ and the photon momentum k_{photon} [57]:

$$k_{||}^2 = k_{photon}^2 \frac{\varepsilon_r}{\varepsilon_r + 1} \tag{2.3}$$

where ε_r is the dielectric function of the metal relative to the dielectric function of the dielectricum, i.e., $\varepsilon_r = \varepsilon_{metal}/\varepsilon_{dieletric}$. And the photon momentum is expressed as $k_{photon} = \omega/c$, where c is the speed of light. An important fact reflected by (2.3) is that the momentum of surface plasmons exceeds the momentum of plane waves when the dielectric functions for the metals are strongly negative, which is generally true for metals. One thing we are aware is that the surface plasmons discussed above are coupled oscillations of electron density and electromagnetic field. The suitable term

for is surface plasmon polariton. Surface plasmons are, strictly speaking, the electron density oscillation modes without the coupling with the field [58].

As for deeper discussion of surface plasmon, we can refer to the book by Raether [57] which has a thorough discussion on the mechanism of surface plasmon.

2.1.3 Frequently Used Optical Parameters

As predicted by Drude-Sommerfield model, metallic nanoparticles exhibit striking interaction with incident light and thus we need to pay intense attention to their optical spectra [2]. We suppose a particle is illuminated with the light intensity per area $I_0(\omega)/A$, where $I_0(\omega)$ is the intensity of incident lights. Consequently, the light scattering, absorption and extinction of metallic nanoparticles can be expressed as cross-sections in frequency domain, i.e., C_{sca}, C_{abs} and C_{ext}, respectively [51]. We note that $C_{ext} = C_{sca} + C_{abs}$. Furthermore, the amount of scattered light by a metallic nanoparticle is written as:

$$I_{sca}(\omega) = \frac{I_0(\omega)}{A} C_{sca}(\omega) \tag{2.4}$$

Usually, these optical cross-sections are normalized to the nanoparticle's cross-sectional area projected onto a plane perpendicular to the wavevector of incident light as $Q_{sca} = C_{sca}/G$, $Q_{abs} = C_{abs}/G$ and $Q_{ext} = C_{ext}/G = Q_{sca} + Q_{abs}$, which are called as scattering, absorption and extinction efficiencies, where G is the particle cross-sectional area projected onto a plane perpendicular to the incident beam. Within Chapter 3 of Bohren and Huffman [51], the authors have given rigorous deduction and detailed expressions of above-mentioned terms.

2.2 Electrodynamic Theories for Plasmon Resonance of Spherical Metal Particles

In this section, we will give a relatively complete electrodynamic description of plasmon resonance of spherical metal particles, which is the primary focus throughout the research of this thesis. The main goal of the quasi-static approximation for small spherical particles and the description on large spherical particle plasmon resonance is to provide

an intuitive and qualitative method of understanding the plasmon resonance of spherical particles with different sizes. Mie theory, however, aims to delineate a theoretic framework of precisely determining the optical properties of spherical particles.

2.2.1 Quasi-static Approximation for Small Spherical Particle

When the size of a metallic spherical particle is much smaller than the wavelength of incident light, the retardation effect is negligible and the electric field of the light can be taken to be constant, thus the oscillating electric field of metal particle activates the free electrons in the metal particle to oscillate coherently [59, 58]. This is called as quasi-static approximation, or Rayleigh theory [51], where dipole term is dominant. As for a small spherical metallic nanoparticle, we now account for the boundary conditions with Laplace equation of electric field and after a tedious derivation,the electric field outside this spherical nanoparticle can be written as [59]

$$\mathbf{E}_{out} = \mathbf{E}_o\hat{\mathbf{x}} - \alpha\mathbf{E}_o\left[\frac{\hat{\mathbf{x}}}{\mathbf{r}^3} - \frac{3\hat{\mathbf{x}}}{\mathbf{r}^5}(\mathbf{x}\hat{\mathbf{x}} + \mathbf{y}\hat{\mathbf{y}} + \mathbf{z}\hat{\mathbf{z}})\right] \tag{2.5}$$

where $\mathbf{E}_o$ is electric field magnitude of incident light beam, α is the sphere polarizability and $\hat{\mathbf{x}}$, $\hat{\mathbf{y}}$ and $\hat{\mathbf{z}}$ are the usual unit vectors of three perpendicular axes of Cartesian coordinate system.

As for a spherical particle, Laplace equation solutions demonstrate that dipole polarizability is given by

$$\alpha = \mathrm{g}_d r_0^3, \tag{2.6}$$

where r_0 is the radius of spherical particle and g_d is given by Clausius-Mossotti relation as

$$\mathrm{g}_d(\omega) = \frac{\varepsilon(\omega) - \varepsilon_M}{\varepsilon(\omega) + 2\varepsilon_M}, \tag{2.7}$$

where $\varepsilon(\omega)$ is the dielectric function of metallic nanoparticle and ε_M is that of surrounding medium. Furthermore, this radiating dipole formulated by Eq.(2.5)-Eq.(2.7) contributes to extinction and scattering spectra of this spherical particle. The corresponding extinction and scattering efficiencies can be expressed as [59, 3]

$$Q_{ext} = 4x\mathrm{Im}(\mathrm{g}_d), \tag{2.8}$$

and

$$Q_{sca} = \frac{8}{3}x^4|\mathrm{g}_d|^2, \tag{2.9}$$

where Im means the imaginary part of a symbol, $x = k_M r_0 = 2\pi(\varepsilon_M)^{0.5} r_0 \lambda^{-1}$, k_M is the angular wavenumber of incident light propagating in surrounding medium and λ is the wavelength of this incident light.

2.2.2 Large Spherical Particle Plasmon Resonance

When the size of metallic nanoparticle is sufficiently large so that above-mentioned dipole plasmon model can not describe the distribution of associated electromagnetic field, we have to account for higher multipoles terms into the solution of Maxwell's equation because the quadrupole term dominates the extinction and scattering spectra of large spherical nanoparticles [59]. Utilizing same notations as above and considering quadrupole term ($l = 2$) in the Laplace equation solution, $\mathbf{E}_{out}$ now turns into

$$\mathbf{E}_{out} = \mathbf{E}_o\hat{\mathbf{x}} - \alpha\mathbf{E}_o\left[\frac{\hat{\mathbf{x}}}{\mathbf{r}^3} - \frac{3\hat{\mathbf{x}}}{\mathbf{r}^5}(\mathbf{x}\hat{\mathbf{x}} + \mathbf{y}\hat{\mathbf{y}} + \mathbf{z}\hat{\mathbf{z}})\right]$$

$$+j\mathbf{k}\mathbf{E}_0(x\hat{\mathbf{x}} + z\hat{\mathbf{z}}) - \beta\mathbf{E}_o\left[\frac{x\hat{\mathbf{x}} + z\hat{\mathbf{z}}}{\mathbf{r}^5} - \frac{5z}{\mathbf{r}^7}(x^2\hat{\mathbf{x}} + y^2\hat{\mathbf{y}} + xz\hat{\mathbf{z}})\right] \tag{2.10}$$

where the quadrupole term g_q can be written as

$$\mathrm{g}_q(\omega) = \frac{\varepsilon(\omega) - \varepsilon_M}{\varepsilon(\omega) + 3/2\varepsilon_M}, \tag{2.11}$$

which is somewhat different with the coefficients of Eq.(2.7).

Similarly, we can derive the expression of extinction and scattering efficiencies as

$$Q_{ext} = 4x\mathrm{Im}\left[\mathrm{g}_d + \frac{x^2}{12}\mathrm{g}_q + \frac{x^2}{30}(\varepsilon(\omega) - 1)\right] \tag{2.12}$$

and

$$Q_{sca} = \frac{8}{3}x^4 + \left\{\left|\mathrm{g}_d\right|^2 + \frac{x^4}{240}\left|\mathrm{g}_q\right|^2 + \frac{x^4}{900}\left|\varepsilon(\omega) - 1\right|^2\right\} \tag{2.13}$$

2.2.3 Mie Theory

All the size, shape, and environment dependent optical properties of spherical metal nanoparticles are due to their unique intense interaction with incident light beam, or in other words, surface plasmon resonance. These optical properties become understandable and feasible thanks to the elegant work of Gustav Mie, who solved Maxwell's equations for a homogeneous sphere in 1908 [60]. Strictly speaking, Mie scattering theory should be classified as an indispensable corner of classic electrodynamic description of optical spectra of small particles [60, 51]. It is a highly effective and precise method providing the analytic solutions of optical spectra of particles with geometry as sphere and spheroid [61].

Solid Sphere Case

Within Mie theory, expressions for the extinction, scattering and absorption efficiencies for spherical particles that are subject to a beam of linearly polarized incident light are written as:

$$Q_{ext} = \frac{2}{x^2}\sum_{n=1}^{\infty}(2n+1)\mathrm{Re}(a_n + b_n), \tag{2.14}$$

and

$$Q_{sca} = \frac{2}{x^2}\sum_{n=1}^{\infty}(2n+1)\{|a_n|^2 + |b_n|^2\}. \tag{2.15}$$

where Re represents the real part of a symbol.

Furthermore, because extinction is simply the sum of the absorption and scattering efficiencies, i.e. $Q_{ext} = Q_{abs} + Q_{sca}$, the absorption efficiency can be written as

$$Q_{abs} = \frac{2}{x^2}\sum_{n=1}^{\infty}(2n+1)\left\{\mathrm{Re}(a_n) - |a_n|^2 + \mathrm{Re}(b_n) - |b_n|^2\right\}, \tag{2.16}$$

where magnetic susceptibility a_n is

$$a_n = \frac{s\psi_n(sx)\psi_n'(x) - \psi_n(x)\psi_n'(sx)}{s\psi_n(sx)\zeta_n'(x) - \psi_n'(sx)\zeta_n(x)}, \tag{2.17}$$

and corresponding electric susceptibility b_n is

$$b_n = \frac{\psi_n(sx)\psi_n'(x) - s\psi_n(x)\psi_n'(sx)}{\psi_n(sx)\zeta_n'(x) - s\psi_n(sx)\zeta_n(x)}, \tag{2.18}$$

where s is the refractive index of the sphere, $x = 2\pi(\varepsilon_M)^{0.5} r_0 \lambda^{-1}$, r_0 is the radius of the sphere, λ is the wavelength of the incident beam of light, ε_M is the dielectric function of the surrounding medium, and ψ_n and ζ_n are Riccati-Bessel functions [51].

At this point, we can write the local electric field at position $\tilde{\mathbf{r}}$ close to the surface [3]

$$\begin{aligned}\mathbf{E_{out}}(\tilde{\mathbf{r}}) \quad &= \mathbf{E}_0 \textstyle\sum_{n,m}\{A_{nm}\mathbf{M}^{(1)}_{nm}(k_M, \tilde{\mathbf{r}}) + B_{nm}\mathbf{N}^{(1)}_{nm}(k_M, \tilde{\mathbf{r}}) \\ &+ C_{nm}\mathbf{M}^{(3)}_{nm}(k_M, \tilde{\mathbf{r}}) + D_{nm}\mathbf{N}^{(3)}_{nm}(k_M, \tilde{\mathbf{r}})\}, \end{aligned} \tag{2.19}$$

where $\mathbf{M}_{nm}$ and $\mathbf{N}_{nm}$ can be expressed in terms of vector spherical harmonics(VSH) as

$$\mathbf{M}^{(l)}_{nm}(k, \tilde{\mathbf{r}}) = \nabla \times (\zeta^{(l)}_{nm}(k, \tilde{\mathbf{r}})\tilde{\mathbf{r}}) \tag{2.20}$$

and

$$\mathbf{N}^{(l)}_{nm}(k, \tilde{\mathbf{r}}) = \frac{1}{k}\nabla \times \mathbf{M}^{(l)}_{nm}(k, \tilde{\mathbf{r}}) \tag{2.21}$$

where

$$\zeta^{(1)}_{nm}(k, \tilde{\mathbf{r}}) = \frac{1}{\sqrt{n(n+1)}} z^l_n(kr) Y_{nm}(\theta, \phi), \tag{2.22}$$

where $z^l_n(kr)$ is spherical Bessel function; when $l = 1$, it is spherical Bessel function of the first kind, when $l = 3$, it is spherical Bessel function of the third kind. And $Y_{nm}(\theta, \phi)$ is spherical harmonics given by

$$Y_{nm}(\theta, \phi) = \sqrt{\frac{2n+1}{4\pi}\binom{n+m}{n-m}} P^m_n(\cos(\theta)) \exp(\mathrm{j}m\phi) \tag{2.23}$$

where $P^m_n(\cos(\theta))$ are the associated Legendre functions [3].

According to Chapter 4 of Bohren and Huffman [51], we have A_{nm} and B_{nm} as

$$A_{nm} = -i\mathrm{E}_0 j^n \frac{2n+1}{n(n+1)} \tag{2.24}$$

and

$$B_{nm} = \mathrm{E}_0 j^n \frac{2n+1}{n(n+1)} \tag{2.25}$$

and

$$C_{nm} = a_n A_{nm} \tag{2.26}$$

and

$$D_{nm} = b_n B_{nm} \tag{2.27}$$

The detailed deduction and expressions for A_{nm},B_{nm},C_{nm},D_{nm}, $\mathbf{M}_{nm}$ and $\mathbf{N}_{nm}$ can also be found in Appendix H of Le Ru and Etchegoin [3], which demonstrates all the contents of mathematical deduction. Furthermore, if we take the SERS enhancement factor as fourth order power enhancement of the local electric field [62], we have

$$\rho(\tilde{\mathbf{r}}, \omega) = \left| \frac{\mathbf{E}(\tilde{\mathbf{r}}, \omega)}{E_{inc}(\omega)} \right|^4, \tag{2.28}$$

where ρ is the SERS enhancement factor, $E_{inc}(\omega)$ is the local electric field due to the incident plane wave, and $\mathbf{E}(\tilde{\mathbf{r}}, \omega)$ is the total electric field at position $\tilde{\mathbf{r}}$. We note that ρ is the quantity of interest for Raman-based single molecule detection within the chemistry community [63, 64].

Multi-Layer Sphere Case

Though metallic nanospheres are very popular in nanotechnology, concentric multi-layer metallic nanospheres is ideal in biomedical applications. Thus it is highly desirable to figure out how to determine the optical spectra of general concentric multi-layer spheres. Actually, this goal can be achieved by extending above-mentioned classic, or solid sphere case Mie theory. In Appendix H of Le Ru and Etchegoin [3] there is a detailed deduction of this topic and we now selectively present the outline of this theory.

Without loss of generality, we now consider $i = 1...M$ spherical surfaces with radii r_i. Correspondingly, we have thus delimited $M + 1$ volumes V_i with $i \in \{0, M\}$ and $r_i \leq r \leq r_{i+1}$, where $r_0 = 0$ and $r_{M+1} = \infty$. Obviously, V_1 is a sphere and V_i is a spherical shell for $1 < i \leq M$. The wavevector in each V_i is defined as $k_i = \sqrt{\epsilon_i(\omega)}\omega/c$. Similarly to the case of a single sphere, the spherical symmetry of the problem suggests that we should expand the electric field in each volume in terms of VSHs. Because most volumes do not contain the origin or infinity, the most general expansion of electric field is in terms of $\mathbf{M}_{nm}^{(l)}$ and $\mathbf{N}_{nm}^{(l)}$, where $l = 1, 3$. In volume V_i, the electric field is given by

$$\begin{aligned} \mathbf{E}(\tilde{\mathbf{r}}) \quad &= \mathbf{E}_0 \textstyle\sum_{n,m} \{\alpha_{nm}^{(i)} \mathbf{M}_{nm}^{(1)}(k_i, \tilde{\mathbf{r}}) + \beta_{nm}^{(i)} \mathbf{N}_{nm}^{(1)}(k_i, \tilde{\mathbf{r}}) \\ &+ \gamma_{nm}^{(i)} \mathbf{M}_{nm}^{(3)}(k_i, \tilde{\mathbf{r}}) + \delta_{nm}^{(i)} \mathbf{N}_{nm}^{(3)}(k_i, \tilde{\mathbf{r}})\}, \end{aligned} \tag{2.29}$$

Following the single sphere case, we know that $\gamma_{nm}^{(1)} = \delta_{nm}^{(1)} = 0$ for the inner core sphere. As for the V_i when $i > 1$, $\alpha_{nm}^{(i)} = A_{nm}$ in Eq.(2.24) and $\beta_{nm}^{(i)} = B_{nm}$ in Eq.(2.25), hence both of which are known; while $\gamma_{nm}^{(i)} = C_{nm}$ in Eq.(2.26) and $\delta_{nm}^{(i)} = D_{nm}$ in Eq.(2.27) are unknown and need to be determined.

Now we can start from the boundary conditions on first interface between the inner core sphere with radius r_1 and the spherical shell with radius r_2 to deduce the susceptibilities δ_{nm}^2 and γ_{nm}^2 for the spherical shell with radius r_2 as:

$$\gamma_{nm}^{(2)} = a_n \alpha_{nm}^{(2)}, \text{and} \delta_{nm}^{(2)} = b_n \beta_{nm}^{(2)} \tag{2.30}$$

where a_n and b_n are the susceptibilities of the inner core sphere defined in Eqs.(2.17-2.18). By recursively using the boundary conditions on each interface between the two adjacent spherical shells with radius r_{i-1} and r_i, we can arrive at

$$\gamma_{nm}^{(i)} = a_n^{(i)} \alpha_{nm}^{(i)}, \text{and} \delta_{nm}^{(i)} = b_n^{(i)} \beta_{nm}^{(i)} \tag{2.31}$$

where the new proportionality coefficients are defined as:

$$a_n^{(1)} = b_n^{(1)} = 0, \tag{2.32}$$

and by recurrence on $i = 2...M$

$$a_n^{(i)} = u_n^{(i)} / v_n^{(i)}, \tag{2.33}$$

with

$$\begin{aligned} u_n^{(i)} &= \left[\psi_n(s_i x_i) + a_n^{(i-1)} \zeta_n'(s_i x_i)\right] \psi_n'(x_i) \\ &- s_i \psi_n(x_i) \left[\psi_n'(s_i x_i) + a_n^{(i-1)} \zeta_n(s_i x_i)\right] \end{aligned} \tag{2.34}$$

and

$$\begin{aligned} v_n^{(i)} &= s_i \zeta_n(x_i) \left[\psi_n'(s_i x_i) + a_n^{(i-1)} \zeta_n'(s_i x_i)\right] \\ &- \left[\psi_n(s_i x_i) + a_n^{(i-1)} \zeta_n(s_i x_i)\right] \zeta_n'(x_i), \end{aligned} \tag{2.35}$$

while

$$b_n^{(i)} = \mu_n^{(i)}/\nu_n^{(i)} \tag{2.36}$$

with

$$\begin{aligned}\mu_n^{(i)} &= \psi_n(x_i)\left[\psi_n'(s_i x_i) + b_n^{(i-1)}\zeta_n'(s_i x_i)\right] \\ &-s_i\left[\psi_n(s_i x_i) + b_n^{(i-1)}\zeta_n(s_i x_i)\right]\psi_n'(x_i),\end{aligned} \tag{2.37}$$

and

$$\begin{aligned}\nu_n^{(i)} &= s_i\left[\psi_n(s_i x_i) + b_n^{(i-1)}\zeta_n'(s_i x_i)\right]\zeta_n'(x_i) \\ &-\zeta_n(x_i)\left[\psi_n'(s_i x_i) + b_n^{(i-1)}\zeta_n'(s_i x_i)\right].\end{aligned} \tag{2.38}$$

where ψ_n and ζ_n are Riccati-Bessel functions [51].

Following the Mie theory for solid sphere case, the expressions for extinction, scattering and absorption efficiencies of multi-layer spherical particles subject to a beam of linearly polarized incident light are given by

$$Q_{ext}^{(i)} = \frac{-1}{\pi r_i^2 k_i^2}\sum_{n,m}[|\alpha_{nm}^{(i)}|^2\mathrm{Re}(a_n^{(i)}) + |\beta_{nm}^{(i)}|^2\mathrm{Re}(b_n^{(i)})], \tag{2.39}$$

and

$$Q_{sca}^{(i)} = \frac{1}{\pi r_i^2 k_i^2}\sum_{n,m}[|\alpha_{nm}^{(i)}|^2|a_n^{(i)}|^2 + |\beta_{nm}^{(i)}|^2|b_n^{(i)}|^2]. \tag{2.40}$$

then we can simply express the absorption efficiency as $Q_{abs}^{(i)} = Q_{ext}^{(i)} - Q_{sca}^{(i)}$. Similarly, the near-field SERS factor of multi-layer sphere case is still defined as Eq.(2.28), but the $\mathbf{E}(\tilde{\mathbf{r}}, \omega)$ needs to be updated by Eq.(2.29).

2.3 Strain Effect on Dielectric Function of Metal Nanoparticles

Since one of the topics of this thesis is to utilize the strain effect to enhance the light-trapping performance of PSCs, we now introduce this novel mechanism of how to utilize mechanical strain to tailor the SPR-based optical spectra of metallic nanoparticles

through the strain-corrected dielectric functions. This mechanical strain effect on dielectric functions is the interaction and coupling of two effects, the surface damping effect and the deformation effect on lattice constant. The main part of following discussions is reprinted with permission from X.-H. Qian and H. S. Park, *J. Mech. Phys. Solids* **2010**, *58*(3), 330-345, Copyright 2010 Elsevier [44].

2.3.1 Surface Damping Effect

According to the Drude-Sommelfeld model, the dielectric function of metallic nanoparticles is written as:

$$\epsilon_{bulk}(\omega) = \varepsilon_{core}(\omega) + \varepsilon_{free}(\omega) - 1, \tag{2.41}$$

where the free electron term $\varepsilon_{free}(\omega)$ is written as

$$\epsilon_{free}(\omega) = 1 - \frac{\omega_p^2}{\omega^2 + j\gamma\omega}, \tag{2.42}$$

However, when we deal with metallic nanoparticles with appropriate size, which is around the mean free path of conduction electrons which is around 30-50 nm, we have to account for the size effect into dielectric functions [48, 65]. Specifically, the damping constant in the expression of dielectric functions is size-dependent. Furthermore, the surface damping effect in terms of dielectric function can be treated as, according to [48, 44], the modification of reduced effective mean free path L_{eff} in Eq.(2.42)

$$\gamma(L_{eff}) = \gamma_0 + A\frac{v_F}{L_{eff}}, \tag{2.43}$$

where A is a dimensionless parameter, v_F is the Fermi velocity, and $\gamma_0 = v_F/l_\infty$, where l_∞ is the mean free path of the conduction electrons in the corresponding bulk material. We note that the core electron terms ε_{core} is primarily impacted by this surface damping effect.

Coronado and Schatz [48] have developed a geometric probability approach to calculate L_{eff} for nanostructures of various shapes and sizes, resulting in the analytic expression

$$L_{eff} = 4\frac{V}{S}, \tag{2.44}$$

where S and V are the surface area and the volume of the nanostructure, respectively. The damping that occurs due to the reduced mean free path is assumed to act solely on

the conduction electrons; therefore, the modified bulk dielectric constant in Eq.(2.41) is written as [56, 48]

$$\varepsilon_{bulk}(\omega) = \varepsilon_{core}(\omega) - \frac{\omega_p^2}{\omega^2 + j\omega(\gamma_0 + A\frac{v_F}{L_{eff}})}. \tag{2.45}$$

where the values of all the parameters in above formulas have been given in Table(2.1).

2.3.2 Lattice Deformation Effect for Metal Nanosphere

In addition to surface damping, we now present the formalism by which the effects of mechanical strain are accounted for on the dielectric function of both the core (bound) and conduction (free) electrons via deformation on lattice constant. For the conduction electrons, we follow the work of [49], who noted that due to strain, the plasma frequency ω_p in Eq.(2.41) changes due to the resulting change in free electron density; the plasma frequency can be written for Face-Centered Cubic(FCC) metals as

$$\omega_p^2 = \frac{4e^2}{\varepsilon_0 m_{eff} a^3}, \tag{2.46}$$

where e is the electric charge and a is the deformed, or strained lattice constant of bulk FCC metals; we note that $a_0 = 4.08$ Å is the original, undeformed lattice constant for gold and 4.09 Å for silver. Clearly, any variation in the lattice constant a due to mechanical strain will impact the plasma frequency ω_p, which will result in either a blue or redshift of the optical spectra.

Furthermore, any strain-induced change in lattice constant a also impacts the Fermi velocity v_F in Eq.(2.42); this is because the Fermi energy can be written as

$$E_F = \frac{h^2}{2m}\left(\frac{3}{8\pi}\right)^{2/3} N^{2/3}, \tag{2.47}$$

where h is Planck's constant, m is the electron mass, and N is the electron density. Because the electron density N can be written as, for FCC metals

$$N = \frac{4}{a^3}, \tag{2.48}$$

and noting that the Fermi velocity can be written in terms of the Fermi energy as

$$V_F = \sqrt{\frac{2E_F}{m}}, \tag{2.49}$$

it is clear from Eq.(2.49) that any change in the electron density N due to strain effects on the lattice constant a will change both the Fermi velocity V_F, and the Fermi energy E_F.

However, as discussed by [50], imposed mechanical strain not only affects the dielectric function of the free, or conduction electrons, but also affects the dielectric function for the ionic core, or bound electrons. This can be written as

$$\varepsilon_{core}(\omega) \rightarrow \frac{\varepsilon_{core}(\omega) + 2 + 2\nu(\varepsilon_{core}(\omega) - 1)}{\epsilon_{core}(\omega) + 2 - \nu(\epsilon_{core}(\omega) - 1)}, \tag{2.50}$$

where the constant ν captures the strain-induced change in lattice constant as

$$\nu = \left(\frac{a_0}{a}\right)^3. \tag{2.51}$$

We note that the correction to the dielectric function for the ionic core electrons in Eq.(2.50) is based upon classical theories, which neglect quantum effects such as electron spill out that lead to a blue shift in small metal nanostructures (diameter < 2 nm) with decreasing size. In other words, as discussed by [66], in quantum models due to the spillout effect, fewer electrons are inside the nanoparticle, and therefore fewer electrons are sensitive to the lattice contraction effects on $\varepsilon_{core}(\omega)$ in Eq.(2.50). However, in the present work, the nanoparticle diameters are all 10 nm or greater; therefore, such quantum-driven electron spillout effects can safely be neglected.

In summary, the final classical dielectric functions for FCC metallic nanoparticles are found by modifying the bulk dielectric functions of [55] by accounting for the previously described effects from surface damping [48], lattice deformation effects on the free electron density [49], and lattice deformation effects on the ionic core [50] by combining Eq.(2.45), Eq.(2.46) and Eq.(2.50). And this novel strain-based strategy will be applied in plasmonic solar cells to enhance the light-trapping performance in Chapter 4.

2.3.3 Lattice Deformation Effect for Metal Nanodisc

Previously we presented the methodology of strain-corrected dielectric function for FCC metallic nanosphere, but when the axial surface stress applies on the two ends of a FCC metallic nanodisc which only hosts the two dimensional rotational symmetry, rather than the three dimensional spherical symmetry [46], the strain strategy will be slightly

altered. Specifically, three parameters have to be updated as following

$$\omega_p^2 = \frac{4e^2}{\varepsilon_0 m_{eff} a_0^2 (a_0 \pm \Delta a)}, \tag{2.52}$$

$$N = \frac{4}{a_0^2 (a_0 \pm \Delta a)}, \tag{2.53}$$

and

$$\nu = \left(\frac{a_0}{a_0 \pm a} \right). \tag{2.54}$$

where Δa is the fluctuation of lattice constant induced by the strain due to surface stress, plus $+$ representing tensile strain and minus $-$ mirroring compressive strain. Except the three equations, the theoretic framework and all the other equations keep the same.

Chapter 3

Plasmonics of Hollow Metallic Nanospheres

In this chapter, we will report our numerical results of the optical spectra of the hollow gold and silver nanospheres. The PRWs, far-field optical spectra and near-field optical properties of various HGNs and HSNs will be investigated. Part of following discussion has been published in X.-H. Qian and J. Bai, *J. Comp. Theor. Nanoscience* **2013**, *10*, 2354-2360 [67].

3.1 Calculation Method and Verification

In our study, the outer spherical shell is composed of Au or Ag, the interior spherical core is set as air, and the surrounding medium is set as water which is the dominant component of biological tissue where hollow metallic nanostructures are widely used [27]. The cross section of a typical hollow metallic nanosphere has been plotted in Fig.(1.3) of Chapter 1. We note that, the aspect ratio(AR) α of hollow nanospheres is defined as r_1/r_2, where r_1 represents inner radius and r_2 is overall radius, which is unlike the definitions in circular discs mentioned in next chapter on plasmonic solar cell.

3.1.1 Calculation Method

We employed the Mie theory for multi-layer sphere case introduced in Chapter 2 to calculate the optical spectra of hollow metallic nanospheres, and adopted the SPlaC v1.0 as the calculation bench, which incorporates the Mie solvers for optical properties of single solid sphere, multi-layer sphere and multiple spheres, though current study is not related to the multiple spheres case.

The geometric parameters of hollow metallic nanospheres are given by the overall radii r_2 and AR, which lead to $r_1 = \mathrm{AR} * r_2$, where AR ranges over $[0.1, 0.9]$ with step 0.1 and r_2 spans over $[10, 20, 30, 40, 50, 80, 120, 200, 300, 400]$nm.

As for the dielectric constants of bulk gold and silver, we utilized the experimental data by Johnson and Christy [55], which is listed in Tab.(C.1). Nevertheless, considering our discussion in Chapter 2, the surface damping effect has to be accounted for the dielectric functions of all the how metallic nanosphere and nanoparticles in following chapters under study, unless otherwise notified. Based on formula Eqs.(2.41-2.45) and the physical parameters for gold and silver in Tab.(2.1), we composed a Matlab® function to correct the dielectric constants of bulk gold and silver. The output dielectric constants will be used in Mie theory calculation in SPlaC. The dielectric constant of air is chosen to be $\varepsilon_{air} = 1$ and that of water is $\varepsilon_{water} = 1.77$.

The step of wavelength is chosen to be 1 nm. The maximum iteration steps of SPlaC is set as 50 or 100 dependent on the size of particle.

We then execute a set of commands and SPlaC functions in Matlab® to perform a series of numerical experiments of SPR spectra of HGNs and HSNs, i.e., far-field extinction efficiency and near-field SERS, whose algorithm has been formulated in multi-layer sphere Mie theory of Chapter 2. We know the SPR of metallic nanoparticles is dependent on size, shape, materials of particle and surrounding medium, etc. But in this study we primarily focus on the geometry effects, i.e., the size and shape effects on SPR of hollow metallic nanospheres. Specifically, we quantify the size effect and aspect ratio effect in tuning extinction efficiency spectra, PRWs and SERS of hollow metallic nanospheres.

The calculation procedure can be concisely summarized as following:

1. `Correct the dielectric constants of HGNs and HSNs by surface damping`

effect based on Eqs.(2.41-2.45)

2. Input the geometry parameters, corrected dielectric constants of spherical shell, dielectric constants of inner core and surrounding medium into Matlab

3. Setup the step of wavelength and initiate the parameters of SPlaC

4. Execute appropriate commands and SPlaC functions in Matlab to determine SPR of HGNs and HSNs

5. Post-process the output data of SPlaC, which includes Q_{ext}, Q_{abs}, Q_{sca} and local electric field

In order to clearly convey how we execute this calculation, we include a sample Matlab code of determining the SPR of a HGN in Appendix D.

In particular, when we calculate the SERS factor of hollow metallic nanospheres, we follow the assumption raised in [6] of neglecting the chemical contributions to the SERS enhancement induced by the formation of chemical bonds and the hybridization of electrons between the molecular orbital and the Bloch functions. Instead, only electromagnetic enhancements are considered in our simulations.

3.1.2 Verification on the Validity of Calculation

In order to verify the validity of our source codes, we need to select an adequate data source for check. Since we find the Noguez and Zhang are very vivid in the research on SPR of nanostructures and especially hollow metallic nanoparticles [68, 4, 23], we try to repeat the extinction cross section of a group of concentric spherical gold-core silver-shell nanostructures with varying thickness of the silver-shell δ_{Ag} from 0 nm to 7 nm and fixed diameter of gold-core as 48 nm displayed in Fig. 4 of Roman-Velazquez, *et al* [27]. Then we conduct the Mie theory calculation of these concentric spherical nanoparticles with the surface damping corrected dielectric constants and wavelength step 1 nm via SPlaC. After post-processing, we plot the counterpart extinction cross sections in Fig.(3.1) in comparison with Fig. 4 of [27]. Needless to say, there is an excellent agreement between the two figures. The only difference we note is when δ_{Ag}

increases to be greater than 4 nm, a primary peak appears between 500 nm and 540 nm, while in the original plot, the primary peak diminish as the δ_{Ag} increases and finally disappear when δ_{Ag} reach 7 nm. We ascribe this difference to the treatment of surface damping effect and the choice of the parameters used in surface damping effects, primarily the dimensionless damping constant A, which is theory-dependent parameter, and Fermi velocity v_F. In the work of [27], the authors followed the scheme proposed by Noguez [69] and picked the v_F and A which had been originally used by Kreibig [70, 47].

We have thus demonstrated the reliablity and validity of our source codes and numerical results on the optical properties of hollow spherical metallic nanoparticles. Now we conduct the analysis of our numerical results on the SPR of HGNs and HSNs in forthcoming sections.

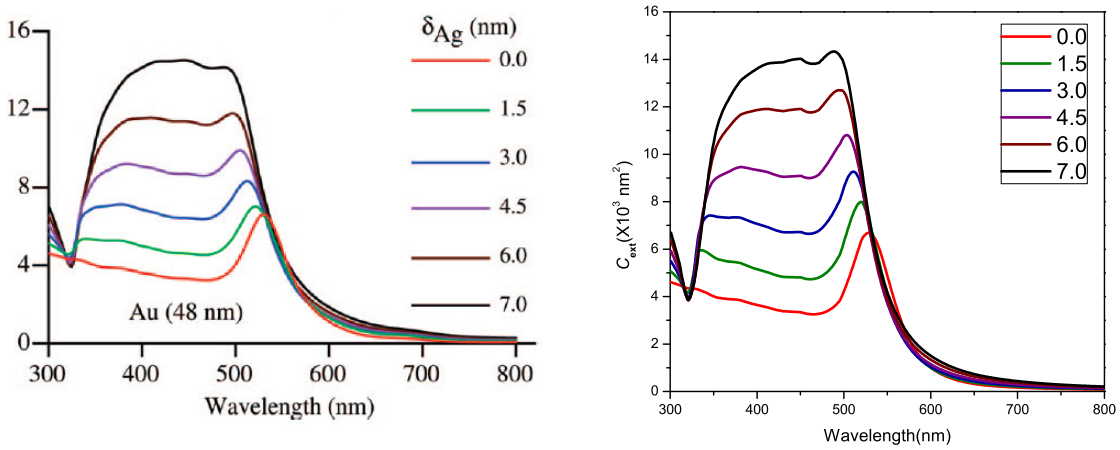

(a) (b)

Figure 3.1: (a) Calculated C_{ext} spectra of gold-silver core-shell spherical NPs immersed in water with gold core diameter of 48 nm and different silver shell thickness from 0 nm to 7 nm (Reprinted with permission from C. E. Roman-Velazquez, C. Noguez and J. Z. Zhang, *J. Phys. Chem. A* **2009**, *113*, 4068-4074. Copyright 2009 American Chemical Society.) (b)The counterpart C_{ext} spectra of exactly same nanoparticle determined by our source codes realized on SPlaC v1.0. C_{ext} in both figures are in unit of $10^3 nm^2$.

3.2 Optical Properties of Hollow Au and Ag Nanospheres

3.2.1 Far-field Extinction Efficiency

The first important characteristic we want to investigate is the far-field spectra of extinction efficiency of HGNs and HSNs. We now plot these extinction efficiency spectra of both nanoshells in Fig.(3.2).

On the basis of the observation of each figure in Fig.(3.2), we delineate a series of common trends of both nanoshells. As for HGNs, the maximum extinction efficiency increases as the size of nanoshells(measured by overall radii) increases and then diminish with increasing size when the overall radius exceeds some critical value. As for the three figures from Fig.(3.2a) to Fig.(3.2c), this critical value is 50 nm. The latter phenomenon is triggered by the size effect which manifests itself in radiation damping [71]. In addition, we observe that as the overall radius increases, the higher order multipolar terms play more important role and thus lead to the broadening of the plasmonic spectra [59]. As we expected, Fig.(3.2d) to Fig.(3.2f) convey that extinction efficiency spectra of HSNs share similar trends that HGNs have. The difference between the extinction spectra of HGNS and HSNs lies in that the critical value of overall radii of HSNs is 10 nm, which is much smaller than that of HGNs. This fact reflects that silver nanostructures are more sensitive to size effect than gold nanostructures do.

We now shift our focus to the effect of AR on optical spectra of these metallic nanoshells. The first common trend owned by both HGNs and HSNs due to the increasing aspect ratio is the increasing peak of almost each extinction efficiency spectra. Secondly, we note that the resonance wavelength of each extinction efficiency spectra experience red shift as the aspect ratio increases. The two trends confirm the prediction of plasmon hybridization theory [37, 72], which points out that increased aspect ratio triggers stronger coupling between the sphere plasmon and cavity plasmon, hence it enhances the splitting between bonding and antibonding hybridization plasmons and thus as can be seen in Figure(3.2), the optically active plasmonic spectra were red shifted.

3.2.2 Plasmon Resonance Wavelength

Considering the important findings of red shift we pointed out in previous discussion, we now focus on the plasmon resonance wavelengths of both types of metallic nanoshells.

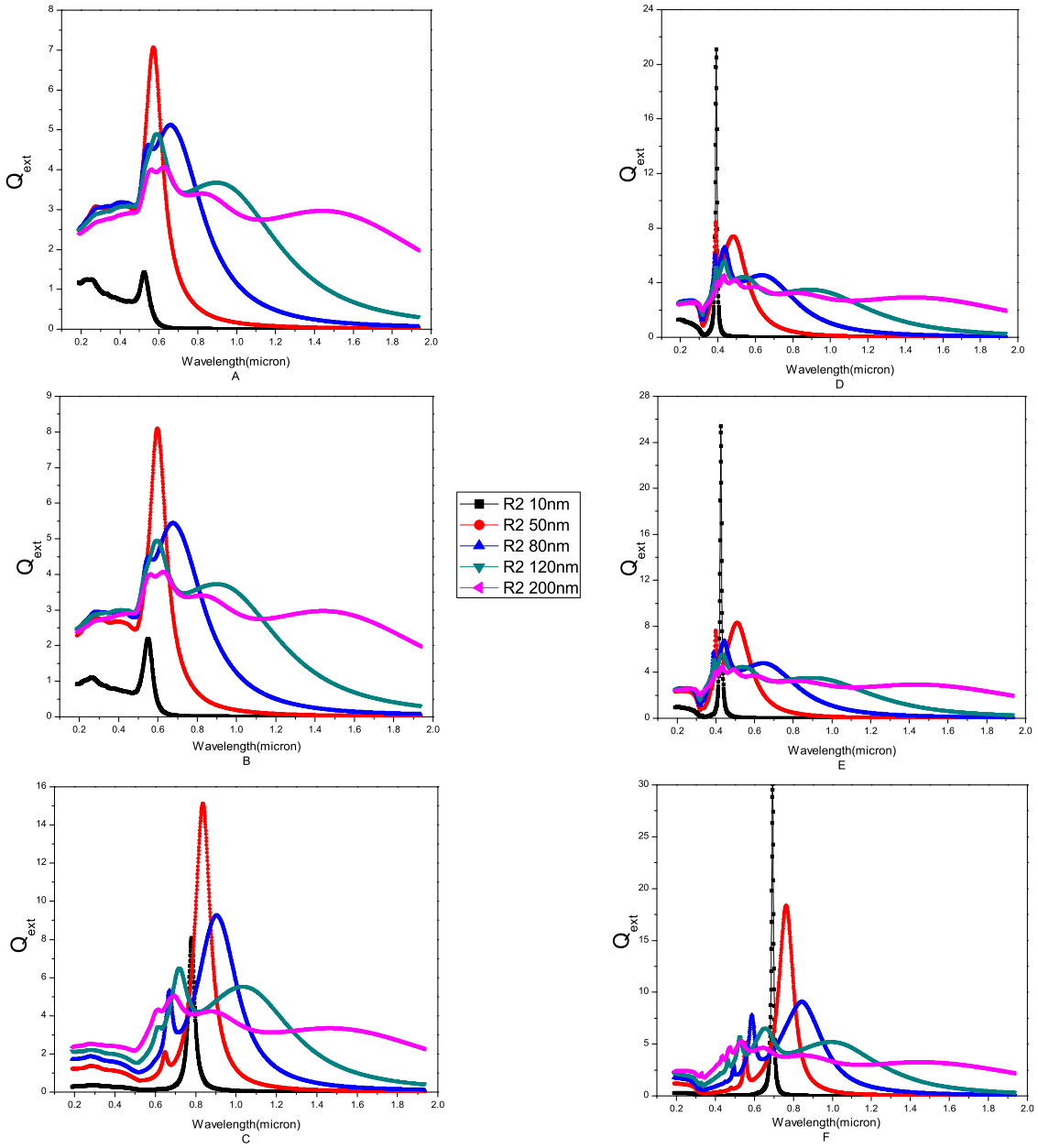

Figure 3.2: The extinction efficiency of a group of nanoshells with different material and geometry. (A) HGNs with AR 0.3 and varying overall radii (B) HGNs with AR 0.6 and varying overall radii (C)HGNs with AR 0.9 and varying overall radii (D) HSNs with AR 0.3 and varying overall radii (E) HGNs with AR 0.6 and varying overall radii (F)HSNs with AR 0.9 and varying overall radii

Please note that in our simulations, we calculate the real plasmon peak and then determine the corresponding resonance wavelength, rather than the dipole plasmon wavelength [38]. In doing so, we aim to correlate our investigation to applications such as biomedical imaging, where people typically utilize the real plasmon peaks.

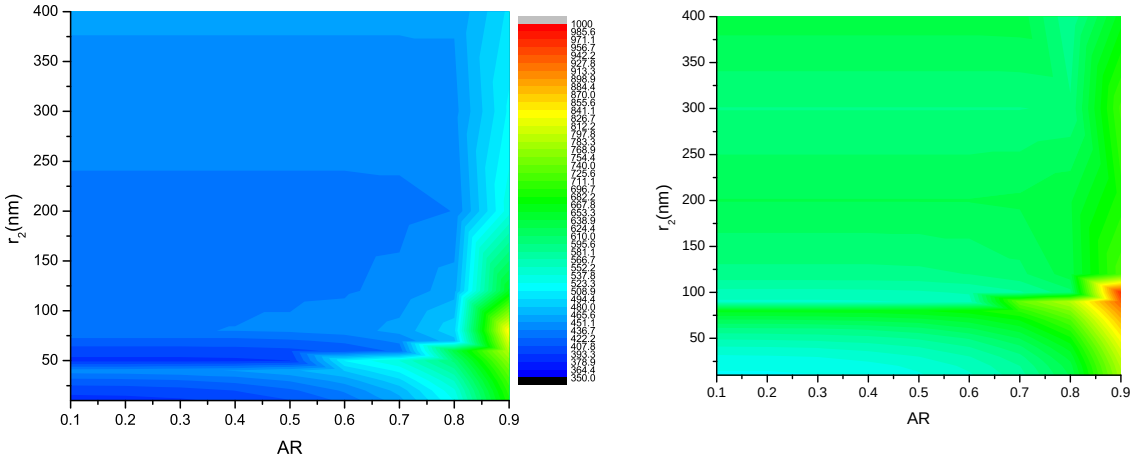

Figure 3.3: (a) PRW distribution of HSNs and (b) PRW distribution of HGNs as functions of overall radii and aspect ratio.

We now plot the plasmon resonance wavelengths(PRWs) of both HSNs and HGNs in Fig.(3.3a) and Fig.(3.3b), respectively. In the this figure, both plots share the same legend, which ranges from 350 nm to 1000 nm. In each plot, the horizontal axis represents the aspect ratio, ranging from 0.1 to 0.9, and the vertical axis is the overall radii of nanoshells, varying from 10nm to 400 nm.There are several important trends conveyed by this figure. The first trend is size effect of nanoshell plays the dominant role in determining the resonance wavelengths. As for both nanoshells, when overall radius is sufficiently large, the PRWs are relatively independent with the aspect ratio. Particularly, however, when the aspect ratio reachs 0.8 and 0.9, the PRWs of both metallic nanoshells possess their maximum values, which increase as size increase. The second fact we note is that the PRWs of HGNs usually exceed that the PRWs of HSNs. In addition, the third characteristic of this contour is that the PRWs distribution of HGNs is steeper and narrower than the distributions of PRWs of HSNs.

We now begin to delineate these trends. Regarding the first trend, as can been in Fig.(3.3a), most PRWs of HSNs keep fixed when the overall radius exceeds 60 nm. This trend is further confirmed by the distribution of PRWs of HGNs conveyed in Fig.(3.3b), where the distribution of PRWs is ideally even and has no fluctuation when the overall radius exceeds 120 nm. This phenomena is directly linked to size effects in terms of two important mechanisms: the dynamic deplorization and radiation damping [71, 59, 3, 45]. The underlying reason for this particularly interesting red shift of resonance wavelength as size increases is the typical retardation effect of noble metallic nanostructures. Specifically, by accounting for the mechanism of SPR we know that the opposite charges of electron clouds covering the surface of metallic nanostructures are separated by the distance almost equal to diameter, and hence the response of one end of these hollow nanospheres to the changes in the other end will delay after their diameter enlarges. Correspondingly, the period of SPR becomes longer, which demands the red shift of resonance wavelength of SPR. Within the frame of Mie theory, this size effect can be understood as the results of higher order electric poles and, in some cases, induced magnetic poles [3].

Regarding the second important fact, Fig.(3.3) mirrors that PRWs of HSNs spans over the band from 350 nm to 800 nm, while the PRWs of HGNs are no less than 500 nm and the maximum of them is 964 nm. As we have noted, SPR-based optical properties with resonance wavelength close to or around NIR is highly desirable in relevant biological applications [34]. Since the geometry of both nanoshells are exactly the same, we ascribe this differences between PRWs of both metallic nanoshells to the distinct intrinsic properties of materials. Furthermore, the existence of interband transition of gold is the main difference between the two metals and triggers the huge difference of the dielectric functions of the two metals, which is directly responsible for the distinct optical properties of the two nanoshells we have observed so far.

3.2.3 Near-field Surface-enhanced Raman Scattering

The other important factor of metallic nanostructures is the Surface-enhanced Raman scattering. In our investigation, the SERS factor is defined as Eq.(2.28). Here we fix $\mathbf{r}_m$ as r_2 to ensure the calculated SERS factor is the quantity of interest for single molecule detection emphasized by the chemistry community [3, 7, 64].

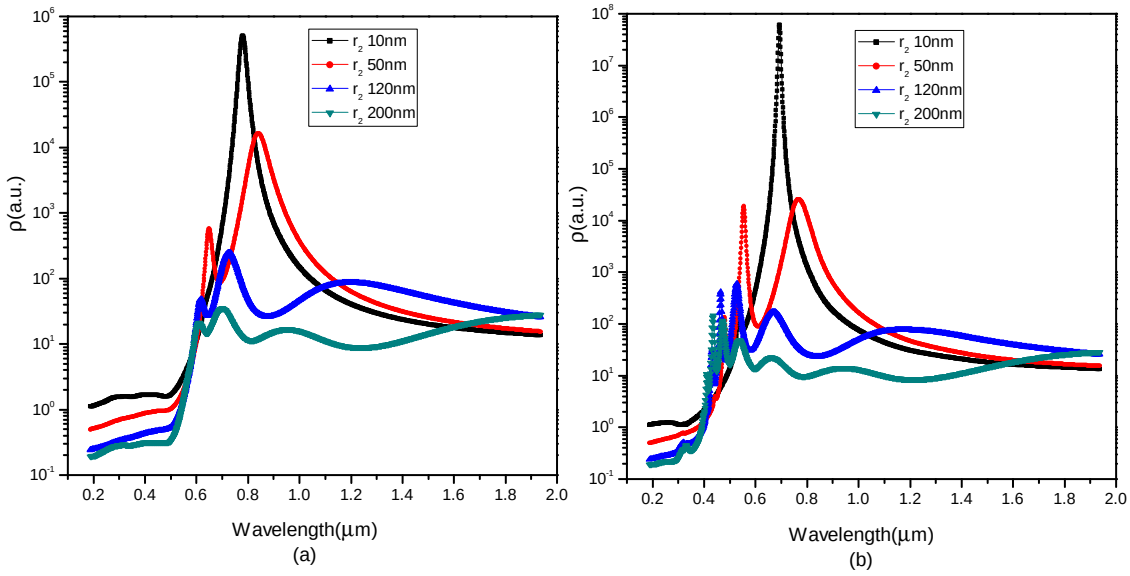

Figure 3.4: (a)SERS of HGNs with AR 0.9 and varying overall radii (b) SERS of HSNs with AR 0.9 and varying overall radii.

In Fig.(3.4), we plot the SERS factors at the surface of both kinds of metallic nanoshells with AR 0.9 and varying size, as of which the strongest plasmon coupling are reported to occur [38]. Fig.(3.4) firstly reflects that ρ reach its maxima of nanoshells with smallest size, i.e., overall radius 10 nm. This is consistent with the observation that radiation damping is significant for nanoparticles with diameters no less than 25 nm[73]. It also hints that SERS enhancement is highly sensitive to the size compared to the extinction efficiency, which can be qualitatively interpreted by the electrostatic approximation theory presented in [3, 45]. The second interesting finding is that the SERS enhancement factor of HSNs in Fig.(3.4b) is generally larger than that factor of HGNs in Fig.(3.4a). This could be understood by considering that silver is more free-electrcon dominant compared with gold [52]. The third significant fact we obtain from Fig.(3.4) is that maxima SERS enhancement factor do not typically occur at dipole

plasmon resonance wavelength, which is asserted in[3]. Actually, they occur at dipolar PRW for small size nanoshells, but occur at lowest quadrupolar peak, or the shoulder peak for large size nanoshells. This interesting phenomenon is still induced by size effect as we have discussed.

Chapter 4

Strain Induced Optical Tunability of Metal Nanoparticles and Plasmonic Solar Cell

In this chapter, we will delineate the mechanical-strain-induced optical tunability and more importantly, the enhancement of SPR of metallic nanoparticles and plasmonic solar cell. We first study the strain-effect on SPR of single FCC metallic nanoparticles. Then we transit to how strain tailor the SPR of a metallic NP array. Simultaneously, we propose and investigate a novel strategy of utilizing the mechanical strain to enhance the light-trapping performance of PSCs. .

4.1 Configuration and Calculation Method

In this section, we first plot the typical geometry of nanospheres and nanodiscs. Secondly, we introduce the procedures of how to determining the strain-corrected dielectric constants of gold and silver NPs. Finally, we describe the procedures of utilizing Mie theory to calculate the SPR of strained metal NPs and employing transfer matrix method(TMM) to simulation optical parameter of the metal NP array on top of PSCs, respectively.

4.1.1 Configuration of Metal Nanoparticles

In current research, two types of FCC metal nanoparticles are under study, the nanosphere and nanodisc with circular cross section in axial direction, which are described in Fig.(4.1).

(a) (b)

Figure 4.1: Geometry of (a) Nanosphere and (b) Nanodisc

As for cylinder, we note there is a special parameter aspect ratio(AR) used to describe the geometry of cylinder, which is defined as h/r, h is the height of cylinder and r is the radius of circular cross section.

In order to fabricate PSCs, we deposit the array of well-engineered gold and silver nanospheres and/or nanodiscs in designated geometry and align them on the top surface of traditional thin-film solar cells [39], then we get PSCs as described in Fig.(1.4).

We note that strain will be applied on those metallic NP array to enhance the light trapping efficiency in following numerical experiments. If the absorption of the top layer of PSC (metallic NP array) is improved by strain, the light-trapping performance of the whole PSC is also enhanced. Furthermore, we are capable of controlling the enhancement via modifying this artificially applied strain.

4.1.2 Strain Corrected Dielectric Functions of Metal Nanoparticles

In this chapter, we study the strain-induced tunability of optical spectra of single FCC metallic nanosphere and nanodisc and the strain-induced light-trapping performance of FCC metallic nanosphere array and nanodisc array deposited on the top of PSCs. Therefore, we firstly determine the strain-corrected dielectric functions of FCC metallic nanosphere and metallic nanodisc.

The dielectric constants of bulk gold and silver are still chosen as the measurement data of Johnson and Christy [55] and can be found in Tab.(C.1), all the necessary physical parameters are listed in Tab.(2.1).

We then incorporate Eqs.(2.41-2.51) to account the strain effect for nanosphere via composing a Matlab® function. For example, if we apply 5% compressive strain, the corresponding lattice constant of FCC metal nanosphere experiences a 5% contraction, and a 5% tensile strain leads to a 5% expansion of lattice constant. Then the strain effect on metallic nanospheres has been included in the output dielectric constants of corresponding Matlab® code we developed.

Similarly, we combine most of the equations among Eqs.(2.41-2.51) to write a Matlab® function to account for the strain effect into dielectric functions of FCC metallic nanodisc. Nevertheless, we note that the axial strain solely induces the change of axial length of nanodisc, i.e., the height in Fig.(4.1. This difference requires us to replace Eq.(2.46) by Eq.(2.52), Eq.(2.48) by Eq.(2.53) and Eq.(2.51) by Eq.(2.54) and keep using the remaining equations among Eqs.(2.41-2.51) when composing the strain-correction code for nanodisc. Consequently, the output dielectric functions include the axial strain effect on FCC metallic nanodisc.

4.1.3 Calculation Method for Single Metal Nanosphere

We still employ Mie theory to calculate the strain-induced effect on SPR spectra of gold and silver nanospheres. Here we fix the radius of bulk case gold and silver nanosphere at 20 nm. When a 5% tensile strain applied on a FCC metallic nanosphere, the radius expands to 1.05 times of original radius, i.e., 21 nm. Similarly, a 5% compressive strain generates a 5% contraction of radius, which turns into 0.95 times original radius, i.e., 19 nm. In other words, the radius of gold and silver nanosphere with radius 20 nm subject

to $[-5\%, 0, 5\%]$ strain is $[19, 20, 21]$ nm, correspondingly.

The surrounding medium is set as air with $\varepsilon_{air} = 1$. The step of wavelength is fixed at 1 nm. With all these preliminary data along with the strain-corrected dielectric functions, we execute the corresponding Matlab® commands provided by SPlaC [3] to conduct the Mie theory calculation of the SPR spectra for strained single gold and silver nanosphere.

4.1.4 Calculation Method for the Top Metal Nanoparticle Array Layer

We note that the PSC is a complex layered structure as described in Fig.(1.4). To the best of our knowledge, TMM is ideally sutiable for simulation of optical parameters of layered structure [74]. We present a concise introduction of the theoretic formulation of TMM in Appendix B. The numerical solver we utilize is ISU-TMM, the three dimension TMM package developed by Li, *et. al.* [75, 76].

The input dielectric constants of metallic nanosphere and nanodisc are strain-corrected dielectric constants from Johnson and Christy [55] as we discussed.

Within our TMM calculations of gold and silver NP array, the reference length is chosen to be 1 μm, the wavelength step is set as 0.02 μm. The polarization angle is set as zero and propagation of incident light wave is set in z axis direction, and is normal to metallic NP array on PSCs. The plane wave number in both x axis direction and y axis direction is set as 15, real space grid resolution in both x axis direction and y axis direction is set as 51. All these configurations can guarantee the TMM calculation is convergent.

4.2 Strain Tuned Optical Spectra of Metal Nanospheres

We now focus on the analysis of the impact on plasmon resonance and associated optical parameters. In order to reveal the strain-effect on plasmon of nanoparticle array which will be utilized to enhance the light trapping of PSC, we now begin with the analysis of strain effect on single spherical metallic NP and will extend this strain effect on metallic NP array in next section.

We first show the results of 5% compressive and 5% tensile strain effect on scattering efficiency of spherical gold and silver nanoparticles with radius 20 nm.

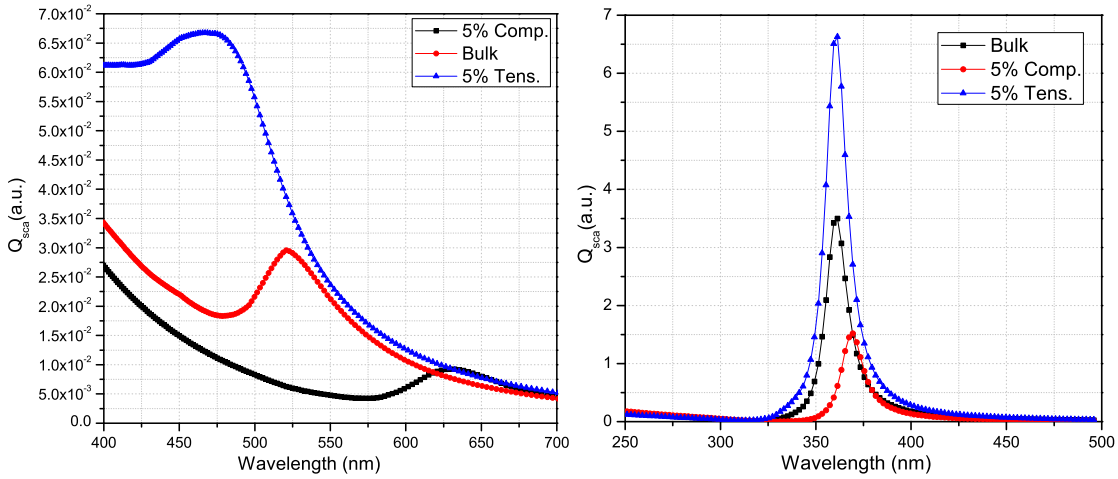

(a) (b)

Figure 4.2: Strain-corrected scattering efficiency (a)silver nanosphere and (b)gold nanosphere(both with bulk case diameter 20 nm) as function of strain.

There are several valuable trends observed from the two metallic nanospheres which we will address one by one. The first common trend for the scattering efficiency of both nanoparticles is that tensile strain increases the scattering while compressive strain reduces the scattering. Secondly, we find that the PRWs have been shifted due to the strain, where compressive strain leads to redshift and tensile strain results in blueshift. The underlying mechanism of the strong strain-dependence of scattering efficiency or similar optical properties of metallic nanoparticle lies in that interband transitions of core electrons from the valence band to the Fermi surface of metal dominates the PR of metallic nanoparticle in visible spectrum [77, 78, 79, 44]. Besides, compared to gold nanosphere, we note that the PRW of bulk silver nanosphere is almost unshifted by strain. This is due to the fact that blueshift stemming from increased free electron density is essentially balanced by the redshift generated by the enlargement of the core electron dielectric function [50]. This phenomenon is linked to the difference between the PRWs of metallic nanoparticles and the interband transition wavelength of the bulk metal. Specifically, the PRW of gold nanosphere appears around 525 nm, which is almost coincident with interband transition wavelength of gold at 515 nm, hence strain significantly impact the bound electron contribution to dielectric function of gold. In

contrast, the PRW of silver nanosphere occurs around 360 nm, which does not overlap with the interband transition wavelength of silver at 330 nm [55].

4.3 Strain Enhanced Light Trapping of Plasmonic Solar Cell

Most of the following contents has been published in X.-H. Qian and J. Bai, *37th IEEE Photovoltaic Specialist Conference* **2011**, *Seattle*.

In this section, we will investigate the strain effect on the metallic nanoparticles array deposited on the top layer of PSC. We have given a sufficient introduction to the strain-corrected methodology in Chapter 2. By virtue of this modification, SPR and associated far-field and near-field optical properties such as PRWs, extinction, scattering, absorption and SERS are all impacted. We now begin the analysis of numerical results calculated via TMM simulation, and focus on the light trapping performace of Au and Ag nanosphere and nanodisc array deposited on PSCs subject to strain.

In order to clearly demonstrate the strain effect, we now define a strain-induced yield factor in percentage as following

$$\eta_{parameter} = 100(\frac{Q^{strain}}{Q^{bulk}} - 1). \tag{4.1}$$

where Q^{bulk} represents some general parameter of bulk nanoparticles and Q^{strain} represents that general parameter of strained nanoparticles.

We firstly focus on the strain-induced light trapping performance of metal nanosphere array. Fig.(4.3a) conveys the significant influence of 5% compressive strain on the yield of absorption of gold and silver nanosphere array. Specifically, we find that 5% compressive strain improve the absorption of gold nanosphere array composed with identical single nanosphere with diameter 20nm by the yield from 21.62% to 24.20%, and the absorption of similar array of gold nanosphere with diameter 25nm by 19.82% to 22.82%. In comparison, Fig. (4.3b) reflects that due to 5% compression, the absorption of two silver nanoparticle arrays with same size are enhanced by around 22% and 19%, respectively. These huge yield 20%-25% of absorption are crucial to PSC and is able to reduce the thickness of semiconductor layers and hence to save the cost of solar cell industry. The other important finding we want to stress is the slopes of yield curves

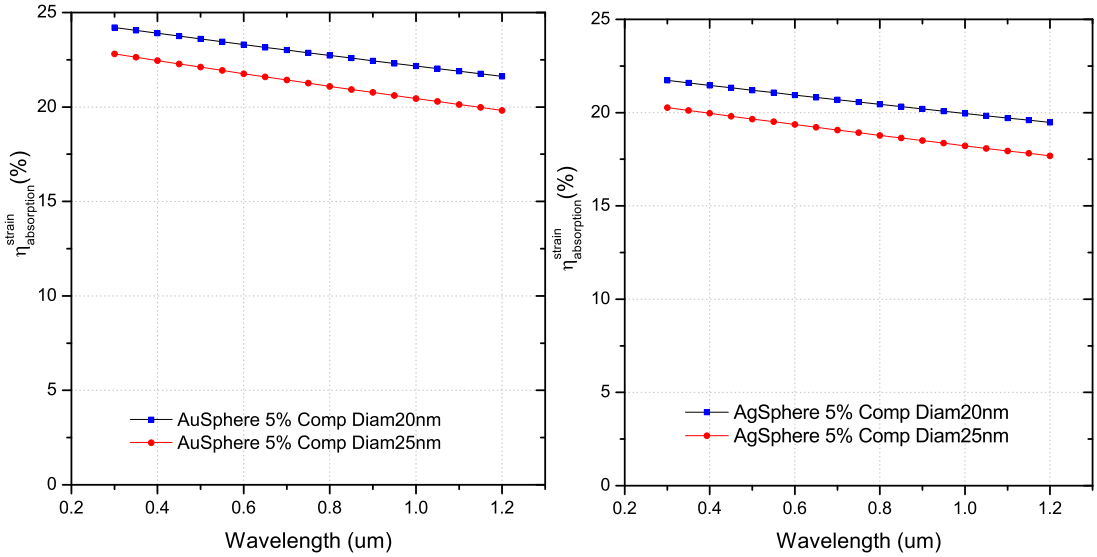

(a) (b)

Figure 4.3: Plots of (a) 5% compressive strain induced absorption yield of array of gold nanosphere with diameter 20 nm and 25 nm and (b) 5% compressive strain induced absorption yield of silver nanosphere with diameter 20 nm and 25 nm on top of PSC.

are sufficiently small as the wavelength of incident sunlight varies from 0.3 μm to 1.2 μm, which is the solar spectrum around the radiation peak window. Being broadband stable is a critical technical index to be achieved in the design of solar cells. Besides, the reason we choose the sizes of nanosphere in our array as 20nm and 25nm lies in that strain effects are strong with these sizes [44, 45].

Meanwhile, a valuable and particular phenomenon we note from Fig.(4.3) is that, in contrast to the tensile strain enhancing the optical parameters of single metallic nanoparticle, 5% compressive strain raises the absorption of PSC while tensile strain weakens that of PSC. To be specific, we now plot the absorption of the silver nanosphere array with diameter 20nm single nanosphere of bulk state and of being subject to 5% compressive strain and 5% tensile strain in Fig.(4.4). This phenomenon is in sharp contrast with originally reported strain-effects on single metallic nanoparticles [44, 45, 46] where compressive strain suppresses SPR and tensile strain promotes SPR. The specific underlying mechanism is still under study, we currently ascribe this distinct character to the complex pattern brought by the interaction between strain effect and

the existence of array mode.

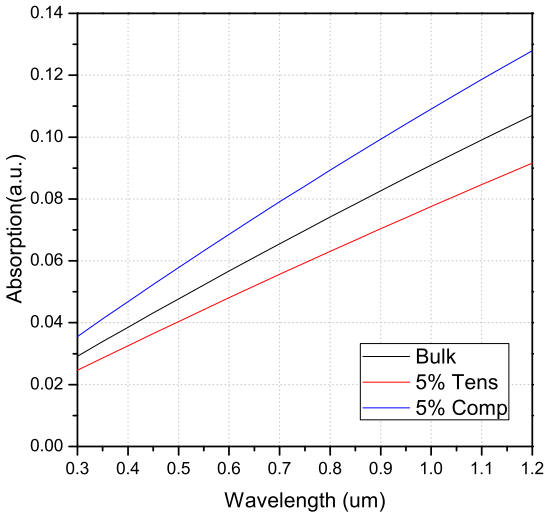

Figure 4.4: Plot of absorption of bulk state, 5% compressive Strain and 5% tensile strain induced absorption of array of silver nanosphere with diameter 20nm on top of a PSC.

We now address the strain effects on metal nanodisc array with circular cross sections deposited on thin-film solar cell. As can be seen from Fig.(4.5), the strain-induced yield of absorption of silver nanodisc array with different combinations of size and aspect ratio spans between 0.8% and 2.1%. The mechanisms being responsible for the weak strain effect on nanodisc array may lie in that surface stress only exist in axial direction of nanodisc, which is two dimension rotationally symmetric, and thus the only one dimension strain itself is more like negligible in comparison with the surface stress applied in all the three directions of nanosphere, which is three dimensional spherically symmetric [44, 45, 46]. In addition, Fig.(4.5) reflects that nanodisc array with higher AR tends to be produce higher strain-induced yield of the absorption, which is originated by the fact that higher AR may induce larger strain-induced correction of the dielectric functions of FCC metallic nanodisc [48]. These numerical experiments suggest that metallic nanodisc array may not be an excellent candidate with the goal of using strain to enhance the quantum efficiency of thin-film plasmonic solar cell. As for the gold nanodisc array, the corresponding strain-induced behavior is similar to above-mentioned silver nanodisc case, but the strain-induced yield is much smaller.

We actually conducted the simulation on larger gold and silver nanosphere and nanodisc array but the strain effect is somewhat weak compared to above results. Specifically, we have not observed that larger sizes metal NP array generate higher strain-induced yield of absorption.

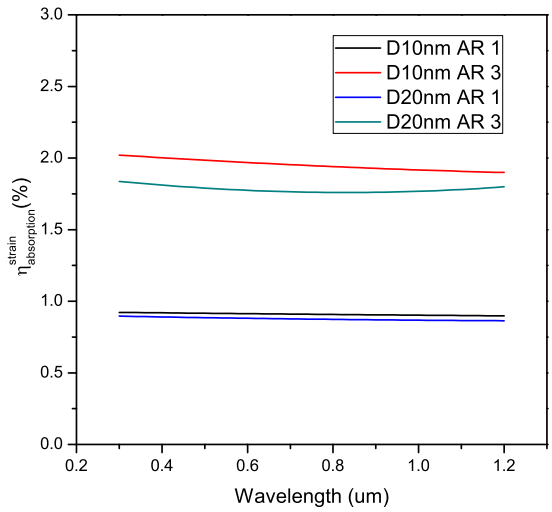

Figure 4.5: 5% tensile strain induced absorption yield of silver nanodisc array with different radii and heights on top of a PSC.

Chapter 5

Conclusion

This thesis is centered on the SPR of nobel metallic NPs, as of which can be categorized as to parts: the general optical properties of hollow gold and silver nanospheres and the methodology of strain-enhanced light-trapping of PSCs. We firstly introduce the application and motivation of current research of SPR in Chapter 1. Chapter 2 is dedicated to the analytical and numerical algorithms we used to conduct calculations of corresponding optical spectra of metallic NPs. We present a detailed analysis of optical spectra generated by the SPR of HGNs and HSNs, such as extinction spectra, PRW distribution as function of geometric parameters of hollow spherical nanospheres in Chapter 3. We then investigate the novel scheme of utilizing the mechanical strain to promote the absorption of metallic NP array deposited on the PSCs in Chapter 4. The main contribution is summarized in following lists:

5.1 Plasmonics of Hollow Metallic Nanospheres

We present a detailed investigation of the far-field and near-field optical properties of HSNs and HGNs. The analysis of extinction efficiency spectra, PRWs and SERS are presented in details. Through these investigations, the general pattern of the optical spectra of hollow metallic NP manifests itself in each of the above-mentioned optical parameters. Furthermore, we reveals an important finding that the tunability of SPR of hollow metallic NPs is dependent on the geometry of themselves and how they are

related. It is crucial that our findings is capable of providing physical insight to the parallel experiments and industrial applications on the optical tunability of hollow metallic NP. In addition, we also find that various filling material of inner core and surrounding medium can impact the SPR spectra of HGNs and HGNs, the peaks of extinction efficiency spectra, the PRWs and the SERS experience some fluctuation. In the future we will conduct a more detailed and profound investigation on the environment effect.

5.2 Strain Enhanced Light Trapping of Plasmonic Solar Cells

We utilize a recently emerging strain-based technique to the metallic NP array on top of PSC to enhance the absorption of PSCs. We firstly show the strain effect the SPR-based optical spectra of single metallic NPs and nanodimer. We then apply the 5% compressive and 5% tensile strain on array of nanodisc and nanosphere, and find that the absorption of both gold and silver nanosphere array subject to 5% strain are enhanced by over than 20% compared to bulk state nanosphere array. On the other hand, gold and silver nanodisc array is able to enhance the optical absorption of PSCs, while the tunability is limited to be within 3%. The shape effect in conjunction with array effect lead to the reduction of tunability of nanodisc array. We also find that enlarged single silver nanodisc will decrease the stain-induced yield of absorption of whole nanodisc array. Currently we just theoretically predict this strain-engineering-based methodology of the top layer of PSCs. In the future, we will conduct three-dimensional full-wavelength simulation including the multiphysical mechanism occurring within the different layers of PSCs and finally compare the results of our numerical experiments with real experiments on PSCs to improve the efficiency of advanced solar cell design and save the fabrication cost.

Bibliography

[1] Wikipedia. surface plasmon, 2013.

[2] E Ozbay. Plasmonics: merging photonics and electronics at nanoscale dimensions. *Science*, 311:189–193, 2006.

[3] E C Le Ru and P G Etchegoin. *Principles of Surface-Enhanced Raman Spectroscopy and related plasmonic effects*. Elsevier, Amsterdam, 2009.

[4] A M Schwartzberg and J-Z Zhang. Novel optical properties and emerging applications of metal nanostructures. *Journal of Physical Chemistry C*, 112(28), 2008.

[5] M Moskovits. Surface-enhanced spectroscopy. *Reviews of Modern Physics*, 57(3):783–826, 1985.

[6] Katrin Kneipp, Martin Moskovits, and Harald (Eds) Kneipp. *Surface-Enhanced Raman Scattering*. Springer, 2006.

[7] S J Oldenburg, R D Averitt, S L Westcott, and N J Halas. Nanoengineering of optical resonances. *Chemical Physics Letters*, 288:243–247, 1998.

[8] L R Hirsch, A M Gobin, A R Lowery, F Tam, R A Drezek, N J Halas, and J L West. Metal nanoshells. *Annals of Biomedical Engineering*, 34(1):15–22, 2006.

[9] Y Sun and Y Xia. Gold and silver nanoparticles: a class of chromophores with colors tunable in the range from 400 to 750 nm. *The Analyst*, 128:686–691, 2003.

[10] W L Barnes, A Dereux, and T W Ebbeson. Surface plasmon subwavelength optics. *Nature*, 424:824–830, 2003.

[11] L R Hirsch, R J Stafford, J A Bankson, S R Sershen, B Rivera, R E Price, J D Hazle, N J Halas, and J L West. Nanoshell-mediated near-infrared thermal therapy of tumors under magnetic resonance guidance. *Proceedings of the National Academy of Science*, 100(23):13549–13554, 2003.

[12] X Huang, I H El-Sayed, W Qian, and M A El-Sayed. Cancer cell imaging and photothermal therapy in the near-infrared region by using gold nanorods. *Journal of the American Chemical Society*, 128(6):2115–2120, 2006.

[13] J J Mock, S J Oldenburg, D R Smith, D A Schultz, and S Schultz. Composite plasmon resonant nanowires. *Nano Letters*, 2(5):465–469, 2002.

[14] N G Khlebtsov and L A Dykman. Optical properties and biomedical applications of plasmonic nanoparticles. *Journal of Quantitative Spectroscopy and Radiative Transfer*, 111:1–35, 2010.

[15] K Sokolov, M Follen, J Aaron, I Pavlova, A Malpica, R Lotan, and R Richards-Kortum. Real-time vital optical imaging of precancer using anti-epidermal growth factor receptor antibodies conjugated to gold nanoparticles. *Cancer Research*, 63:1999–2004, 2003.

[16] I H El-Sayed, X Huang, and M A El-Sayed. Surface plasmon resonance scattering and absorption of anti-EGFR antibody conjugated gold nanoparticles in cancer diagnostics: applications in oral cancer. *Nano Letters*, 5(5):829–834, 2005.

[17] M L Brongersma, J W Hartman, and H A Atwater. Surface plasmon subwavelength optics. *Physical Review B*, 62(24):R16356–R16359, 2000.

[18] S A Maier, M L Brongersma, P G Kik, S Meltzer, A A G Requicha, and H A Atwater. Plasmonics - a route to nanoscale optical devices. *Advanced Materials*, 13(19):1501–1505, 2001.

[19] M Hu, X Wang, G Hartland, V S-M, and L Liz-Marzan. Heat dissipation in goldsilica core-shell nanoparticle. *Chemical Physics Letters*, 372:767–772, 2003.

[20] S Link and M El-Sayed. Optical properties and ultrafast dynamics of metallic nanocrystals. *Annual Review of Physical Chemistry*, 54:331–366, 2003.

[21] J Hodak, A Henglein, and G Hartland. Photophysics of nanometer sized metal particles: Electron-phonon coupling and coherent excitation of breathing vibrational modes. *Journal of Physical Chemistry B*, 104(43):9954–9965, 2000.

[22] H-S Zhou, I Honma, H Komiyama, and J W Haus. Controlled synthesis and quantum-size effect in gold-coated nanoparticles. *Physical Review B*, 50:12052–12056, Oct 1994.

[23] A M Schwartzberg, T Y Olson, C E Talley, and J-Z Zhang. Synthesis, characterization, and tunable optical properties of hollow gold nanospheres? *Journal of Physical Chemistry B*, 110(40):19935–19944, 2006.

[24] T Y Olson, A M Schwartzberg, C A Orme, C E Talley, B O'Connell, and J-Z Zhang. Hollow gold silver double-shell nanospheres: Structure, optical absorption, and surface-enhanced raman scattering. *Journal of Physical Chemistry C*, 112(16):6319–6329, 2008.

[25] D A Wheeler, R J Newhouse, H-N Wang, S-L Zou, and J-Z Zhang. Optical properties and persistent spectral hole burning of near infrared-absorbing hollow gold nanospheres. *Journal of Physical Chemistry C*, 114(42):18126–18133, 2010.

[26] M A Mahmoud, B Snyder, and M A El-Sayed. Surface plasmon fields and coupling in the hollow gold nanoparticles and surface-enhanced raman spectroscopy. theory and experiment. *Journal of Physical Chemistry C*, 114(16):7436–7443, 2010.

[27] C E Roman-Velazquez, C Noguez, and J-Z Zhang. Theoretical study of surface plasmon resonances in hollow gold?silver double-shell nanostructures? *Journal of Physical Chemistry A*, 113(16):4068–4074, 2009.

[28] S J Oldenburg, S L Westcott, R D Averitt, and N J Halas. Surface enhanced raman scattering in the near infrared using metal nanoshell substrates. *Journal of Chemical Physics*, 111(10):4729–4735, 1999.

[29] S Preciado-Flores, D-C Wang, D A Wheeler, R Newhouse, J K Hensel, A Schwartzberg, L-H Wang, J-J Zhu, M Barboza-Flores, and J-Z Zhang. Highly

reproducible synthesis of hollow gold nanospheres with near infrared surface plasmon absorption using pvp as stabilizing agent. *Journal of Materials Chemistry*, 21:2344–2350, 2011.

[30] F Le, D W Brandl, Y A Urzhumov, Hui Wang, Janardan Kundu, Naomi J. Halas, Javier Aizpurua, and Peter Nordlander. Metallic nanoparticle arrays: A common substrate for both surface-enhanced raman scattering and surface-enhanced infrared absorption. *ACS Nano*, 2(4):707–718, 2008.

[31] R Bardhan, N K Grady, and N J Halas. Nanoscale control of near-infrared fluorescence enhancement using au nanoshells. *Small*, 4(10):1716–1722, 2008.

[32] S-W Kim, M Kim, W Y Lee, and T Hyeon. Fabrication of hollow palladium spheres and their successful application to the recyclable heterogeneous catalyst for suzuki coupling reactions. *Journal of the American Chemical Society*, 124(26):7642–7643, 2002.

[33] W Lu, G-D Zhang, R Zhang, L G Flores, Q Huang, J G Gelovani, and C Li. Tumor site-specific silencing of nf-kappab p65 by targeted hollow gold nanosphere-mediated photothermal transfection. *Cancer Research*, 70(8):3177–3188, 2010.

[34] R Weissleder. A clearer vision for *in vivo* imaging. *Nature Biotechnology*, 19:316–317, 2001.

[35] A B Moshe and G Markovich. Synthesis of single crystal hollow silver nanoparticles in a fast reaction-diffusion process. *Chemistry of Materials*, 23(5):1239–1245, 2011.

[36] H-P Liang, L-J Wan, C-L Bai, and L Jiang. Gold hollow nanospheres: Tunable surface plasmon resonance controlled by interior-cavity sizes. *Journal of Physical Chemistry B*, 109(16):7795–7800, 2005.

[37] E Prodan and P Nordlander. Plasmon hybridization in spherical nanoparticles. 120(11):5444–5454, 2004.

[38] F Tam, A Chen, J Kundu, H Wang, and N Halas. Mesoscopic nanoshells: Geometry-dependent plasmon resonances beyond the quasistatic limit. *Journal of Chemical Physics*, 127(204703), 2007.

[39] Zi Ouyang. *Electron-Beam Evaporated Polycrystalline Silicon Thin-film Solar Cells: Paths to Better Performance*. PhD thesis, The University of New South Wales, 2011.

[40] P Spinelli, V E Ferry, J van de Groep, M van Lare, M A Verschuuren, R E I Schropp, H A Atwater, and A Polman. Plasmonic light trapping in thin-film si solar cells. *Journal of Optics*, 14:024002, 2012.

[41] H A Atwater and A Polman. Plasmonics for improved photovoltaic devices. *Nature Materials*, 9:205–213, 2010.

[42] K R Catchpole and A Polman. Plasmonic solar cells. *Optical Express*, 16(26):21793–21800, 2008.

[43] Z Ouyang, S Pillai, F Beck, O Kunz, S Varlamov, K R Catchpole, P Campbell, and M A Green. Effective light trapping in polycrystalline silicon thin-film solar cells by means of rear localized surface plasmons. *Applied Physics Letters*, 96(26):261109, 2010.

[44] X-H Qian and H S Park. The influence of mechanical strain on the optical properties of spherical gold nanoparticles. *Journal of the Mechanics and Physics of Solids*, 58:330–345, 2010.

[45] X-H Qian and H S Park. Strain effects on the SERS enhancements for spherical silver nanoparticles. *Nanotechnology*, 21(36):365704, 2010.

[46] H S Park and X-H Qian. Surface stress driven lattice contraction effects on the extinction spectra of ultrasmall silver nanowires. *Journal of Physical Chemistry C*, 114:8471–8478, 2010.

[47] U Kreibig and M Vollmer. *Optical properties of metal clusters*. Springer-Verlag, 1995.

[48] E A Coronado and G C Schatz. Surface plasmon broadening for arbitrary shape nanoparticles: a geometrical probability approach. *Journal of Chemical Physics*, 119(7):3926–3934, 2003.

[49] W Cai, H Hofmeister, and M Dubiel. Importance of lattice contraction in surface plasmon resonance shift for free and embedded silver particles. *European Physical Journal D*, 13:245–253, 2001.

[50] J Lerme, M Pellarin, E Cottancin, M Gaudry, M Broyer, N Del Fatti, F Vallee, and C Voisin. Influence of lattice contraction on the optical properties and the electron dynamics in silver clusters. *European Physical Journal D*, 17:213–220, 2001.

[51] C F Bohren and D R Huffman. *Absorption and scattering of light by small particles.* Wiley-Interscience, New York, U.S.A., 1983.

[52] Edward (Eds) Palik. *Handbook of optical constants of solids.* Academic Press, Orlando, 1985.

[53] L Qiu, T A Larson, D Smith, E Vitkin, M D Modell, B A Korgel, K V Sokolov, E B Hanlon, I Itzkan, and L T Perelman. Observation of plasmon line broadening in single gold nanorods. *Applied Physics Letters*, 93:153106, 2008.

[54] Charles Kittel and Paul McEuen. *Introduction To Solid State Physics.* John Wiley, 2004.

[55] P B Johnson and R W Christy. Optical constants of the noble metals. *Physical Review B*, 6(12):4370–4379, 1972.

[56] H Hovel, S Fritz, A Hilger, U Kreibig, and M Vollmer. Width of cluster plasmon resonances: bulk dielectric functions and chemical interface damping. *Physical Review B*, 48(24):18178–18188, 1993.

[57] H Raether. *Surface Plasmons on Smooth and Rough Surfaces and on Gratings.* Springer-Verlag, 1988.

[58] Carsten Soennichsen. *Plasmons in metal nanostructures.* PhD thesis, Ludwig-Maximilians-University of Munich, 2001.

[59] K L Kelly, E Coronado, L L Zhao, and G C Schatz. The optical properties of metal nanoparticles: the influence of size, shape, and dielectric environment. *Journal of Physical Chemistry B*, 107:668–677, 2003.

[60] G Mie. Contributions to the optics of the turbid media, particularly of colloidal metal solutions. *Royal Aircraft Establishment*, 1908.

[61] Prashant K. Jain. *Plasmons In Assembled Metal Nanostructures: Radiative and Nonradiative Properties, Near-Field Coupling and its Universal Scaling Behavior*. PhD thesis, Georgia Institute of Technology, 2008.

[62] F J Garcia-Vidal and J B Pendry. Collective theory for surface enhanced raman scattering. *Physical Review Letters*, 77(6):1163–1166, 1996.

[63] J N Anker, W P Hall, O Lyandres, N C Shah, J Zhao, and R P Van Duyne. Biosensing with plasmonic nanosensors. *Nature Materials*, 7:442–453, 2008.

[64] E Hao and G C Schatz. Electromagnetic fields around silver nanoparticles and dimers. *Journal of Chemical Physics*, 120(1):357–366, 2004.

[65] S Link and M A El-Sayed. Spectral properties and relaxation dynamics of surface plasmon electronic oscillations in gold and silver nanodots and nanorods. *Journal of Physical Chemistry B*, 103:8410–8426, 1999.

[66] A Liebsch. Surface-plasmon dispersion and size dependence of Mie resonance: silver versus simple metals. *Physical Review B*, 48(15):11317–11328, 1993.

[67] X.-H. Qian and J. Bai. Theoretical studies of the optical properties of hollow spherical metallic nanoshells. *Journal of Computational and Theoretical Nanoscience*, 10:2354–2360, 2013.

[68] J Z Zhang and C Noguez. Plasmonic optical properties and applications of metal nanostructures. *Plasmonics*, 3(4):127–150, 2008.

[69] C Noguez. Surface plasmons on metal nanoparticles: the influence of shape and physical environment. *Journal of Physical Chemistry C*, 111:3806–3819, 2007.

[70] U Kreibig. Electronic properties of small silver particles: the optical constants and their temperature dependence. *Journal of Physics F: Metal Physics*, 4(7):999–1014, 1974.

[71] A Wokaun, J P Gordon, and P F Liao. Radiation damping in surface-enhanced raman scattering. *Physical Review Letters*, 48(14):957–960, 1982.

[72] H Wang, D W Brandl, P Nordlander, and N J Halas. Plasmonic nanostructures: Artificial molecules. *Accounts of Chemical Research*, 40(1):53–62, 2007.

[73] M Meier and A Wokaun. Enhanced fields on large metal particles: dynamic depolarization. *Optics Letters*, 8(11):581–583, 1983.

[74] Ming Li. *The study of electromagnetic wave propagation in photonic crystal via plane wave based transfer(scattering) matrix method with active gain material applications*. PhD thesis, Iowa State University, 2007.

[75] M Li, X-H Hu, Z Ye, K-M Ho, J-R Cao, and M Miyawaki. Higher-order incidence transfer matrix method used in three-dimensional photonic crystal coupled-resonator array simulation. *Optics Letter*, 31:3498–3500, 2006.

[76] M Li, Z-Y Li, K-M Ho, J-R Cao, and M Miyawaki. High-efficiency calculations for three-dimensional photonic crystal cavities. *Optics Letter*, 31:262–264, 2006.

[77] H Wang, F Tam, N K Grady, and N J Halas. Cu nanoshells: Effects of interband transitions on the nanoparticle plasmon resonance. *The Journal of Physical Chemistry B*, 109:18218–18222, 2005.

[78] P G Etchegoin, E C Le Ru, and M Meyer. An analytic model for the optical properties of gold. *The Journal of Chemical Physics*, 125(16):164705, 2006.

[79] K-S Lee and M A El-Sayed. Gold and silver nanoparticles in sensing and imaging: sensitivity of plasmon response to size, shape, and metal composition. *Journal of Physical Chemistry B*, 110:19220–19225, 2006.

[80] L-L Lin, Z-Y Li, and K-M Ho. Lattice symmetry applied in transfer-matrix methods for photonic crystals. *Journal of Applied Physics*, 94:811–821, 2003.

[81] E M Purcell and C R Pennypacker. Scattering and absorption of light by nonspherical dielectric grains. *Astrophysics Journal*, 1986:705–714, 1973.

[82] K-S Lee and M A El-Sayed. Dependence of the enhanced optical scattering efficiency relative to that of absorption for gold metal nanorods on aspect ratio, size, end-cap shape, and medium refractive index. *Journal of Physical Chemistry B*, 109:20331–20338, 2005.

[83] B T Draine and P J Flatau. Discrete-dipole approximation for scattering calculations. *Journal of the Optical Society of America A*, 11(4):1491–1499, 1994.

Appendix A

Glossary and Acronyms

Care has been taken in this thesis to minimize the use of jargon and acronyms, but this cannot always be achieved. This appendix defines jargon terms in a glossary, and contains a table of acronyms and their meaning.

A.1 Acronyms

Table A.1: Acronyms

Acronym	Meaning
AR	Aspect Ratio
DDA	Discrete Dipole Approximation
FCC	Face-Centered Cubic
GMM	Generalized Multiparticle Mie
HSN	Hollow Silver Nanoshell
HGN	Hollow Gold Nanoshell
PR	Plasmon Resonance
NIR	Near-Infrared Region
NP	Nanoparticle
PRW	Plasmon Resonance Wavelength

Continued on next page

Table A.1 – continued from previous page

Acronym	Meaning
PSC	Plasmonic Solar Cell
SPR	Surface Plasmon Resonance
SERS	surface-enhanced Raman scattering
TMM	Transfer Matrix Method
VSH	vector spherical harmonics

Appendix B

Numerical Methods

B.1 Concept of Transfer Matrix Method

We now introduce the numerical method used in Chapter 4. The transfer matrix method(TMM) is widely used in the numerical analysis of photonic crystal structures [76, 75]. Actually, it is also an effective numerical tool to determine the optical spectra for any objects with some sort of layer structures, which includes the other topic of this thesis, the thin film plasmonic solar cell. There are two types of TMM which differ in the choice of basis functions [80]. We here only adopt the one with plane wave basis functions. We now selectively present the framework of TMM, for those who are interested, detailed derivation of TMM can be found in [74]. We firstly assume that the medium that light encounters is passive and non-magnetic material. The second assumption of TMM is that electric and magnetic field are harmonic. The two assumptions permit us to transform the Maxwell's equations from time domain into frequency domain. After arrangement, we have the frequency-domain Maxwell's equations

$$\nabla \times \tilde{\mathbf{E}}(\tilde{\mathbf{r}}) = ik_0 \tilde{\mathbf{H}}(\tilde{\mathbf{r}})$$

$$\nabla \times \tilde{\mathbf{H}}(\tilde{\mathbf{r}}) = -ik_0 \varepsilon(\tilde{\mathbf{r}}) \tilde{\mathbf{E}}(\tilde{\mathbf{r}}) \tag{B.1}$$

where $k_0 = 2\pi/\lambda_0$ is the wave number of electromagnetic wave in free space, $\tilde{\mathbf{E}}$ and $\tilde{\mathbf{H}}$ are electric field vector and magnetic field vector, respectively. Then we expand the frequency domain Maxwell's equations into reciprocal Fourier space, which then turn

into linear algebra equations. And from now on, all the symbols are in Fourier space, unless otherwise notified. We assign the direction of incident light propagation as Z axis of a Cartesian coordinate system, then after some derivations we reach

$$\begin{bmatrix} \vec{E}(z) \\ \vec{H}(z) \end{bmatrix} = \begin{bmatrix} \mathbf{S}_0 & \mathbf{S}_0 \\ \mathbf{T}_0 & -\mathbf{T}_0 \end{bmatrix} \begin{bmatrix} \vec{E}_0^+(z) \\ \vec{E}_0^-(z) \end{bmatrix} \tag{B.2}$$

where $\vec{E}(z)$ and $\vec{H}(z)$ are field vectors, $\vec{E}_0^+(z)$ and $\vec{E}_0^-(z)$ are the superposition vector of the eigenvectors of linear algebra field equations on the two contrary propagation directions along Z axis, $\mathbf{S}_0$ is identical matrix and block diagonal matrix $\mathbf{T}_0$ is composed of the incident wave vector coefficients, whose element at ith row and jth column is expressed as

$$\mathbf{T}_0^{ij} = \frac{1}{k_0 \beta_{ij}} \begin{bmatrix} -k_{ij,x}k_{ij,y} & k_{ij,x}^2 - \beta_{ij}^2 \\ -k_{ij,y}^2 + \beta_{ij}^2 & k_{ij,x}k_{ij,y} \end{bmatrix} \tag{B.3}$$

where $k_{ij,x}$ and $k_{ij,y}$ are the projection components of corresponding lateral wave vector k_{ij} in x axis and y axis,respecively. β is the eigenvalue of the linear algebra equations of the electrical field in propagation direcion of wave in Fourier space notation [74].

Then we can establish the transfer matrix and scattering matrix. Suppose an object has been sliced into n layers, then the transfer matrix of this object is

$$\mathbf{T} = \mathbf{T}_n \mathbf{T}_{n-1} \dots \mathbf{T}_1 \tag{B.4}$$

where $\mathbf{T}_i$ represents the transfer matrix of the ith layer.

Furthermore, we can relate the transmission, reflection of a layered structure to the transferred scattering matrix as following:

$$T = \frac{|\mathbf{E^t} \times \mathbf{H^t}|}{|\mathbf{E_0} \times \mathbf{H_0}|} = \sum_{ij} \frac{|E_{ij}^t|^2 |\beta_{ij}|}{|E_0|^2 |k_{0z}|},$$

$$R = \frac{|\mathbf{E^r} \times \mathbf{H^r}|}{|\mathbf{E_0} \times \mathbf{H_0}|} = \sum_{ij} \frac{|E_{ij}^r|^2 |\beta_{ij}|}{|E_0|^2 |k_{0z}|},$$

$$A = 1 - T - R. \tag{B.5}$$

where $k_0 \mathbf{H} = \mathbf{k} \times \mathbf{E}$, $\mathbf{k}$ is wave vector, A is absorption, T is transmission and R is reflection. By means of Eq(B.5), we can obtain the transmission and absorption of object subject to incident light beam.

B.2 Concept of Discrete Dipole Approximation

With the goal of providing a comparison to TMM, we make a concise introduction to discrete dipole approximation(DDA), a numerical method widely utilized to calculate the optical spectra of nanoparticles with random geometry.

DDA was originally proposed by Purcell and Pennypacker [81]. The fundamental idea behind this method is to discretize a volume of arbitrary geometry using small (finite) elements, in which each element represents an individual dipole with polarizability α_i that interacts, due to an incident electric field, with all other dipoles in the body. The polarization vector at can be written as [82]

$$\tilde{\mathbf{P}}_i = \alpha_i \tilde{\mathbf{E}}_{loc}(\tilde{\mathbf{r}}_i), \tag{B.6}$$

where dipole polarizability α_i can be written as

$$\alpha_i = \frac{3d^3}{4\pi} \frac{\varepsilon_i - 1}{\varepsilon_i + 2} \tag{B.7}$$

where ϵ_i is the dielectric function of the target material at location $\tilde{\mathbf{r}}_i$. The local electric field vector $\tilde{\mathbf{E}}_{loc,i}$ at location $\tilde{\mathbf{r}}_i$ is the sum of an incident field $\tilde{\mathbf{E}}_{inc,i}$ and the contribution of electric field $\tilde{\mathbf{E}}_{other,j}$ from all the other dipoles in different location $\tilde{\mathbf{r}}_j$ and can be written as

$$\tilde{\mathbf{E}}_{loc,i} = \tilde{\mathbf{E}}_{inc,i} + \tilde{\mathbf{E}}_{other,j} = \tilde{\mathbf{E}}_0 \exp\left(i\tilde{\mathbf{k}} \cdot \tilde{\mathbf{r}}_i - i\omega t\right) - \sum_{j \neq i} \mathbf{A}_{ij} \cdot \tilde{\mathbf{P}}_j, \tag{B.8}$$

where $\tilde{\mathbf{k}}$ is the wave vector of the incident plane wave, $\tilde{\mathbf{E}}_0$ is the amplitude of the plane wave. The vector $\mathbf{A}_{ij} \cdot \tilde{\mathbf{P}}_j$ is the electric field vector at $\vec{r}_i$ due to $\tilde{\mathbf{P}}_j$ at a different location $\vec{r}_j$, including retardation effects. where $\mathbf{A}_{ij}$ is a 3×3 matrix and can be expressed as

$$\mathbf{A}_{ij} = \frac{\exp\left(ikr_{ij}\right)}{r_{ij}} \times \left[k^2(\hat{r}_{ij}\hat{r}_{ij} - \mathbf{I}_3) + \frac{1 - ikr_{ij}}{r_{ij}^2}(3\hat{r}_{ij}\hat{r}_{ij} - \mathbf{I}_3) \right] \tag{B.9}$$

where $k = \omega/c$, $r_{ij} = |\tilde{\mathbf{r}}_i - \tilde{\mathbf{r}}_j|$ and $\hat{r}_{ij} = (\tilde{\mathbf{r}}_i - \tilde{\mathbf{r}}_j)/r_{ij}$. $\mathbf{I}_3$ is identity matrix of size 3.

Now we can determine $\tilde{\mathbf{P}}_j$ by solving following linear equation

$$\sum_{j=1}^{N} \mathbf{A}_{ij} \tilde{\mathbf{P}}_j = \tilde{\mathbf{E}}_{inc,j}. \tag{B.10}$$

Once $\tilde{\mathbf{P}}_j$ is solved, we can evaluate the extinction cross section and absorption cross section as [83]

$$C_{ext} = \frac{4\pi k}{|\tilde{\mathbf{E}}_0|^2} \sum_{j=1}^{N} \mathrm{Im}(\tilde{\mathbf{E}}^*_{inc,j} \cdot \tilde{\mathbf{P}}_j). \tag{B.11}$$

and

$$C_{abs} = \frac{4\pi k}{|\mathbf{E}_0|^2} \sum_{j=1}^{N} (\mathrm{Im}[\tilde{\mathbf{P}}_j \cdot (\alpha_j^{-1})^* \tilde{\mathbf{P}}^*_j]) \tag{B.12}$$

Correspondingly, scattering cross section is calculated as $C_{sca} = C_{ext} - C_{abs}$.

Appendix C

Dielectric Constants of Noble Metal

The complex refractive index of material is expressed as

$$\eta = n + j\kappa \tag{C.1}$$

Now we list the refractive index of gold and silver as functions of wavelength, which are taken from the measurements by Johnson and Christy [55].

Table C.1: Refractive index of gold and silver

$\lambda(\mu m)$	n_{Au}	κ_{Au}	n_{Ag}	κ_{Ag}
0.1879	1.28	1.188	1.07	1.212
0.1916	1.32	1.203	1.10	1.232
0.1953	1.34	1.226	1.12	1.255
0.1993	1.33	1.251	1.14	1.277
0.2033	1.33	1.277	1.15	1.296
0.2073	1.30	1.304	1.18	1.312
0.2119	1.30	1.350	1.20	1.325
0.2164	1.30	1.387	1.22	1.336
0.2214	1.30	1.427	1.25	1.342

Continued on next page

Table C.1 – continued from previous page

$\lambda(\mu m)$	n_{Au}	κ_{Au}	n_{Ag}	κ_{Ag}
0.2262	1.31	1.460	1.26	1.344
0.2313	1.30	1.497	1.28	1.357
0.2371	1.32	1.536	1.28	1.367
0.2426	1.32	1.577	1.30	1.378
0.2490	1.33	1.631	1.31	1.389
0.2551	1.33	1.688	1.33	1.393
0.2616	1.35	1.749	1.35	1.387
0.2689	1.38	1.803	1.38	1.372
0.2761	1.43	1.847	1.41	1.331
0.2844	1.47	1.869	1.41	1.264
0.2924	1.49	1.878	1.39	1.161
0.3009	1.53	1.889	1.34	0.964
0.3107	1.53	1.893	1.13	0.616
0.3204	1.54	1.898	0.81	0.392
0.3315	1.48	1.883	0.17	0.829
0.3425	1.48	1.871	0.14	1.142
0.3542	1.50	1.866	0.10	1.419
0.3679	1.48	1.895	0.07	1.657
0.3815	1.46	1.933	0.05	1.864
0.3974	1.47	1.952	0.05	2.070
0.4133	1.46	1.958	0.05	2.275
0.4305	1.45	1.948	0.04	2.462
0.4509	1.38	1.914	0.04	2.657
0.4714	1.31	1.849	0.05	2.869
0.4959	1.04	1.833	0.05	3.093
0.5209	0.62	2.081	0.05	3.324
0.5486	0.43	2.455	0.06	3.586
0.5821	0.29	2.863	0.05	3.858
0.6168	0.21	3.272	0.06	4.152

Continued on next page

Table C.1 – continued from previous page

$\lambda(\mu m)$	n_{Au}	κ_{Au}	n_{Ag}	κ_{Ag}
0.6595	0.14	3.697	0.05	4.483
0.7045	0.13	4.103	0.04	4.838
0.7560	0.14	4.542	0.03	5.242
0.8211	0.16	5.083	0.04	5.727
0.8920	0.17	5.663	0.04	6.312
0.9840	0.22	6.350	0.04	6.992
1.0876	0.27	7.150	0.04	7.795
1.2155	0.35	8.145	0.09	8.828
1.3931	0.43	9.519	0.13	10.100
1.6102	0.56	11.21	0.15	11.850
1.9373	0.92	13.78	0.24	14.040

Appendix D

Matlab code of Mie Calculation of Hollow Metal Nanospheres

In order to demonstrate our calculation procedure, we have thus included a Matlab code which is responsible for determining the SPR of a hollow metallic gold nanospheres as following

```
%% Initialization
clear all;
global noCheckSum;
% Activate the error-checking
noCheckSum = false;
Nmax = 50; % N_{max} for Mie series

%% Input parameters of hollow metal nanospheres
% refractive index of air-filled core
epsilonCore = 1.0;
 % refractive index of water- host medium
epsilonM = 1.77;
% Set waveleng1 nm per step,which gives
%1750 wavelength points on 0.188-1.937 micron
Nwave = 1750;
```

```
% Setup geometry
% R2 is overall radius
R2 = [10, 20, 30, 40, 50, 60, 70, 80, 90, 100,...
        120, 200, 300, 400]; % in units of nm
AR = 0.1 : 0.1 : 0.9;  % Core-shell aspect ratio

% R1 is inner radius
R1 = zeros( size(AR,2), size(R2,2) );
for i = 1 : size( AR, 2 )
    R1( i, : ) = AR( i ) * R2;
end

% Define a data structure to record the maximum of
% each spectra which might be or not the peak of SPR.
roughPeaks = struct('peakExt',zeros(size( AR, 2 ),size( R2, 2 )),...
'peakAbs',zeros(size( AR, 2 ),size( R2, 2 )),...
 'peakSca',zeros(size( AR, 2 ),size( R2, 2 )),...
 'peakMLoc',zeros(size( AR, 2 ),size( R2, 2 )) );

for v = 1 : size( R2, 2 )
    for u = 1 : size( AR, 2 )

% The file name 'au' specify the material as Gold
[wave, ReEps_bulk, ImEps_bulk] = textread(...
['m_au_JC.dat'],'%f %f %f', Nwave);

% convert wavelength from micron to nm
lambda = wave * 1000;

eps_bulk = ReEps_bulk + j * ImEps_bulk;
% Setup the shell region by specifying inner
```

```
% and outer radii of spherical shell
Shell={ R1( u, v ), R2(v) };
% The dielectric constants array of inner core
% shell and host medium
SEpsilon={epsilonCore, eps_bulk, epsilonM};

%% Mie Calculation of Hollow Metallic Nanospheres
stM_bulk = MulPweSolveMultiSphere(...
    Nmax,Shell, lambda, SEpsilon);

%% Post-procession
Qsca = stM_bulk.Qsca;
Qabs = stM_bulk.Qabs;
Qext = stM_bulk.Qext;
MLocAve = stM_bulk.MLocAve;

   end %v
end %u
```